

Magnetic Fields in Star-Forming Molecular Clouds. II. The Depolarization Effect in the OM C-3 Filament of Orion A

Brenda C. Matthews

McMaster University, 1280 Main Street West, Hamilton Ontario, Canada L8S 4M1

matthews@physics.mcmaster.ca

Christine D. Wilson

McMaster University, 1280 Main Street West, Hamilton Ontario, Canada L8S 4M1

wilson@physics.mcmaster.ca

Jason D. Fiege

Canadian Institute for Theoretical Astrophysics, University of Toronto, Toronto, ON M5S 3H3

fiege@cita.utoronto.ca

ABSTRACT

Polarized 850 μ m thermal emission data of the region OM C-3 in the Orion A molecular cloud are presented. These data, taken in 1998 with the SCUBA polarimeter mounted on the James Clerk Maxwell Telescope, have been re-reduced using improved software. The polarization pattern is not suggestive of a uniform field structure local to OM C-3, nor does the orientation of the vectors align with existing polarimetry maps of the OM C-1 core 20° to the south. The depolarization toward high intensity regions cannot be explained by uniform field geometry except in the presence of changing grain structure, which is most likely to occur in regions of high density or temperature (i.e. the embedded cores). The depolarization in fact occurs along the length of the filamentary structure of OM C-3 and is not limited to the vicinity of the bright cores. Such a polarization pattern is predicted by helical field models for filamentary clouds. Along 75% of the filament's length, the polarization vectors correlate strongly with the filament axis, a signature of a toroidally dominated helical magnetic field; however, near the southern cores, the vectors are offset in direction by 90° from the gas structure of the Integral-shaped Filament, as traced by dust. We present three scenarios to explain the observed polarization pattern of OM C-3 in terms of a

helical field geometry. A helical field which is toroidally dominated in the north and poloidally dominated in the south could wrap the filament. A criss-crossing of two filamentary structures could produce the observed offset in polarization vectors, or the filament could be bent into the plane of the sky. Qualitative models incorporating a helical field geometry are presented for each of the latter two cases.

Subject headings: ISM : clouds, magnetic fields, molecules | polarization | stars: formation | submillimeter

1. Introduction

One of the outstanding questions in the study of star formation concerns the relative importance of magnetic fields in the formation and evolution of clouds, cores and finally protostars. Magnetic fields are thought to provide support against gravitational collapse on large scales, even regulating the filamentary structures observed within molecular clouds (e.g. Fiege & Pudritz (2000a); Carlqvist & Kristen (1997); Nakamura, Hanawa & Nakano 1993). The process of ambipolar diffusion has been proposed to regulate the collapse of dense cores to form protostars (see Shu, Adams & Lizano (1987)). However, some magnetic field must be retained within the protostellar system, since models predict that protostellar outflows are collimated by magnetic fields (e.g. Pudritz (1985); Uchida & Shibata (1985); Shu et al. (1994); Fiege & Hendricksen (1996)). Girart, Crutcher & Rao (1999) present polarization observations of the CO $J = 2 - 1$ line from outflow of the NGC 1333 IRAS 4A which predict the same magnetic field direction as their dust polarimetry at 1.3 mm, at least very close to the outflow source. Further from the source, the outflow is not aligned with the inferred field direction, and this could be due to interaction between the field and outflow. A alignment between the outflow and the field of the outflow has been observed in NGC 2024 FIR 5 (Greaves, Holland & Ward-Thompson 2001) using polarized spectral line observations. The most common method of estimating field strengths has been the detection of Zeeman splitting of atomic and molecular lines. Measurement of Zeeman splitting of the H I 21 cm line provides direct evidence for magnetic fields on very large scales in the Galaxy and in the envelopes of molecular cloud complexes such as Orion A (Heiles 1987). Similar observations with molecular species within dense cores has proven challenging, with detections toward only 15 cloud cores (Crutcher 1999). The sensitivity does not yet exist to measure the Zeeman effect in more tenuous regions of molecular clouds, where the current generation of polarizers are beginning to probe.

Emission from aligned, spinning dust grains is anisotropic and hence polarized. Po-

polarization data reveal no direct information about the field strength, since the degree of polarization is dependent on other factors such as grain shape, composition, and degree of alignment. The degree of polarization is in essence a measure of how effectively the grains have been "spun up" (Hildebrand et al. 1999). Even in theories where the grain spin is induced by a mechanism other than the magnetic field, such as the radiation field (Draine & Weingartner 1996) or the production of H_2 on the grain surface (Purcell 1979), the magnetic field is expected to provide the alignment. Because of this, continuum polarization data are the principal means of probing the geometry of the magnetic field. Each individual dust grain produces polarized emission perpendicular to its local field direction. All polarization data probe only the plane-of-sky component of the three dimensional magnetic field (perhaps vexingly denoted B_{ϕ} , or B_{pos}), but the polarization vectors measured may be either parallel or perpendicular to B_{ϕ} , depending on whether the polarization data are due to absorption of background light by dust grains ($\lambda < 25 \mu\text{m}$), or thermal emission from the grains themselves ($\lambda > 25 \mu\text{m}$). Hildebrand (1988) contains a thorough review. At far-infrared and submillimeter wavelengths, dust emission is optically thin toward all but the densest cores. Therefore, observations represent the sum of polarizations contributed by all dust grains through the depth of the cloud along a line of sight.

Where field geometries are simple and the direction of the magnetic field does not vary through the cloud depth, the polarized emission detected is perpendicular to the mean magnetic field and the latter can be inferred simply by rotating the polarization vectors by 90° . If the field has a more complex, non-uniform geometry, then interpretation becomes more difficult. In such cases, it is best to compare directly the polarization maps with polarization patterns predicted from a physical model of a magnetized cloud. For example, the Integral-shaped Filament of Orion A is clearly filamentary, so core models are inappropriate. Fiege & Pudritz (2000a) present a model for a filamentary cloud in which a helical magnetic field threads the filament and plays an important role in determining the radial density structure. This model predicts an r^{-2} density profile, which has been observed in several clouds, including the Integral-shaped Filament (Johnstone & Bally 1999) and several clouds in Cygnus (Lada, Alves & Lada 1999; Alves, Lada & Lada 1999). Fiege & Pudritz (2000c) present predicted polarization patterns for cases in which the field is either poloidally or toroidally dominated.

Polarimeters aboard the Kuiper Airborne Observatory (KAO), at the Caltech Submillimeter Observatory (CSO) and the James Clerk Maxwell Telescope (JCMT) have detected far-infrared and submillimeter polarization toward many Galactic molecular clouds (Schleuning et al. 1997; Dowell et al. 1998; Schleuning 1998; Aitken et al. 2000; Coppin et al. 2000; Dotson et al. 2000; Matthews & Wilson 2000), although until recently, limitations on detector sensitivity restricted observations to bright and/or compact, usually massive,

cores. Detections of polarized thermal emission from dust have now been made toward individual protostellar envelopes (Girart et al. 1999; Holland et al. 1996) and starless cores (Ward-Thompson et al. 2000). Dotson et al. (2000) contains a summary of all regions toward which polarized emission at 100 μ m was detected with the KAO. Among these sources is OMC-1, a 2000 M \odot core embedded in the Orion A Integral-shaped Filament. These data, along with 350 μ m data from the CSO's Hertz polarimeter, are presented by Schleuning (1998). The polarization pattern observed in OMC-1 has been interpreted as evidence for an hourglass magnetic field geometry, expected if the field is being dragged inward with the gas as the core collapses.

Matthews & Wilson (2000) (hereafter Paper I) presented submillimeter emission polarization data of OMC-3, a 6 $^\circ$ portion of the Integral-shaped Filament of Orion A, located approximately 20 $^\circ$ north of OMC-1. In this follow-up to Paper I, we present an improved polarimetry map as well as a broader discussion of the depolarization observed across the filament. Additionally, we present three possible explanations for the observed polarization pattern, two of which require extensions of the Fiege & Pudritz (2000c) models. Each of these can potentially explain the 90 $^\circ$ offset from the filament axis observed for polarization vectors near OMC-3's southern boundary in terms of magnetic field geometry. The observations and data reduction techniques are described in x2. The polarization data are analyzed in x3. The polarization pattern is interpreted in x4, and x5 contains a discussion and summary.

2. Observations and Data Reduction

Using the SCUPOL polarimeter on the SCUBA detector, 850 μ m maps of polarized thermal emission from dust were obtained on 5 to 7 September 1998 at the James Clerk Maxwell Telescope¹. The data set, polarimeter, and general reduction techniques are described in Paper I, Greaves et al. (2000), and Greaves et al. (2001a). We have re-reduced the data appearing in Paper I using the Starlink software package POLPACK, designed specifically for polarization data obtained with bolometric arrays. The method of reduction remains consistent with our previous analysis, but the new software permits easier binning and filtering of data to extract a higher quality map. Additionally, noisy bolometers have been removed from the data and estimates of the instrumental polarization (IP) have been

¹The JCM T is operated by the Joint Astronomy Centre on behalf of the Particle Physics and Astronomy Research Council of the UK, the Netherlands Organization for Scientific Research, and the National Research Council of Canada.

updated.

At 850 μm , the sky is highly variable on timescales of seconds. This variability must be measured and removed from the data. Chopping removes the effects of slow sky variability; however, fast variations remain in the data, requiring sky subtraction using array bolometers devoid of significant flux. Typically, we have used between one and four bolometers (less than the number used in the reduction of Paper I), depending on the filling factor of the emission across the detector array. It is very difficult to select sky bolometers based on jiggle map data, since bolometers which appear devoid of flux may in fact have negative fluxes if the chop position contained significant emission. This is highly probable in regions of extended emission such as OMC-3. To aid in the identification of bolometers for sky subtraction, we referred to the Johnstone & Bally (1999) scan maps to compare our source and chop position fluxes. If the difference between these two was approximately zero, the bolometers at those locations were candidates for use in sky subtraction. We note that this method will not be generally available in other regions where pre-existing scan maps may not exist. This method prompted us to exclude from sky subtraction some bolometers used in Paper I.

The methods of sky subtraction are discussed in detail in Jenness, Lightfoot & Holland (1998). Prior to sky subtraction, images were made to examine the flux in each bolometer, since bolometers used for sky subtraction should not have negative values (produced if one has chopped onto a location with significant flux, for example). If three bolometers are used, then the signal per second in those three bolometers is averaged and subtracted from each bolometer in the map. Clearly, one should be left with zero flux on average in the sky bolometers. If there is evidence that these bolometers were not completely empty, an estimate of the total flux removed from the map (by summing all the 1s removals) can be made and a fraction of that flux is added back into each bolometer such that the total flux is distributed equally over all 37 bolometers. This assures that the total flux in the map before sky subtraction is the same as after sky subtraction. In the re-reduction for this paper, the mean sky level was added back into the data for OMC-3, thereby avoiding a systematic overestimation of polarization percentage due to underestimates of the total intensity, I . For example, in Paper I, a bolometer which contains a flux almost one quarter that of the MM88 peak was used for sky subtraction. In the extreme case where Q and U are unaffected by the sky removal, this implies that the polarization percentage would be overestimated by a factor of 1.3.

When dealing with extended sources, such as those in OMC-3, the observing technique of chopping from source to a reference position can produce systematic error, since the reference position may not be devoid of flux and may be polarized. Appendix A discusses the

possible in fact such a reference, or chop, position could have on the measured polarization vectors. We particularly want to investigate the so-called "depolarization effect" which refers to the trend, observed in many regions, of measuring lower polarization percentages at positions of high total intensity emission. However, we find that, rather than underestimating the "true" source polarization percentage at high intensity, in fact, chopping onto a region of polarized emission can produce a systematic increase in polarization percentage for regions of low intensity. The degree of increase varies depending on the ratios between the polarized and total fluxes at the reference and source positions. Such an effect would, of course, appear qualitatively identical to the observed "polarization holes". In the scenario we describe, the polarizations at high intensity are most representative of the correct polarization percentage in the source. Similarly, position angles can be adversely affected if the polarized emission from the source and reference positions are oriented differently. Thus, where chopping introduces systematic error, the most reliable polarization percentages and position angles will be observed toward the highest flux positions. For the OMC-3 data set, assuming the reference position is not significantly more polarized than the source, the analysis of Appendix A suggests that even in the faintest regions of the OMC-3 map, the maximum error in the position angles introduced by chopping should range from 10–20%. The slopes of log-log plots of polarization percentage versus intensity observed should not be steeper than -0.3 .

As discussed above, the removal of sky noise is a critical part of reducing SCUBA polarimetry data. Appendix B contains a comparison of reductions with and without sky subtraction for different observations of the same region. Discrepant results are only obtained if no sky subtraction is performed. In fact, whereas non-sky subtracted data tend to show high uniformity in the polarization vectors across the image, the mean polarization position angle differs greatly from one observation to another toward the same region. Once sky subtraction is applied to each map, all the resultant polarization patterns show similar trends.

It is also instructive to subdivide the entire data set and compare one section to another to check for consistency within the data set. For OMC-3, there are a total of 69 individual polarization observations, basically centered on four different positions (see Table 1). We divided the data evenly, so that the S/N per area in the map is maintained across each subset (of 34 and 35 observations respectively). The sky conditions were extremely stable over all three nights, meaning differences in the optical depth should have minimal effects on the S/N of the maps. Polarization maps were then generated for each subset separately, binned to $12''$ and compared. Of the data vectors which had absolute uncertainties in polarization percentage, δp , less than 1.4% and signal-to-noise in polarization percentage, p , greater than 4.2 (values consistent with uncertainties in $\delta p < 1\%$ and $p > 6$ in the total map),

there were 190 vectors in common between the maps. Appendix C contains maps of each subset of data. These maps illustrate that the same general polarization pattern is produced with each subset. Comparison of the percentage polarization data for the 190 vectors in common between the maps reveals that 70% of them show insignificant differences between each other (i.e. $(p_1 - p_2) = (dp_1 + dp_2) < 3$ where we have assumed the errors are correlated in estimating the upper limit on the uncertainty in the difference). The largest discrepancies are seen in the lower intensity regions.

The data presented in this work have lower noise than those in Paper I. Binning the data to $12''$ instead of $6''$ increases the signal-to-noise across the whole map by a factor of 2, since binning is executed in both dimensions. Data are not thresholded by an upper bound on polarization percentage as was done for Paper I. Instead, thresholding is done on total intensity, uncertainty in polarization percentage, and signal-to-noise of polarization percentage. Vectors with low polarization percentage are suspect due to uncertainties in IP values of 0.5% , as well as potential sidelobe contamination (see Greaves et al. (2001b)). For our regions, polarization percentages less than 0.5% are not believable due to sidelobe effects. Thus, to account for these two effects, we reject all vectors with polarization percentage less than 1% . The number of vectors presented in this work is less than that of Paper I, due to higher binning, but the data quality has increased so that we present polarization data toward regions of low total intensity, particularly between the cores MMS6 and MMS7. The mean polarization percentage in Paper I was 4.2% ; the data presented here have a mean of 5.0% . This increase is due to the polarization vectors present in regions originally used for sky subtraction. Their high polarization percentages (particularly in the southern region) increases the new average. We note that even the bolometers used for sky subtraction in this analysis could also contain polarized flux; however, we have utilized Appendix A to estimate the potential effects on our data to be minimal under certain assumptions about the relative polarizing power of and on the bright peaks.

The most substantial change in the polarization pattern from Paper I is in the southern region of the map. As Figure 1 shows, the vectors are on average 30° shifted compared with Paper I. This shift is not exhibited in other regions of the map, and we performed several tests to eliminate potential sources of the shift. Using the same bolometers as in Paper I, we still produce distribution B of Figure 1. We have also tested the effects of the addition of the mean sky flux level back into the map after the removal of sky noise, and the distribution remains unchanged. It is re-assuring that the distribution of vectors we present in this paper is robust against these changes in the reduction procedure and that sky subtraction in POLPACK is not producing the shift. The remaining substantive difference between the reductions we have run for this work and those of Paper I is the use of the POLPACK software itself. Since Paper I was published before POLPACK was available, the Paper I

solution was the result of a "brute force" reduction, which used straight subtraction of fluxes at different waveplate positions to generate the Q and U Stokes' parameters. This method required substantial thresholding to remove data of poor quality and extract the polarization percentages and position angles. Generation of Q and U by subtraction meant that the expected sinusoidal dependence of the flux with waveplate position was not required. In POLPACK, the flux variations with waveplate positions are fit with a sinusoidal distribution and Q and U are extracted from the fit. This method also permits an internal estimation of errors by comparison of equivalent waveplate positions (i.e. 0; 90; 180 and 270 waveplate positions all measure a position angle of 0° on the sky).

The southern region of OMC-3 is distinguished from the rest of the filament by the presence of extended emission of significant unpolarized intensity on either side of the filament. If the solutions for Q and U were under or over-estimated due to extreme values in some bolometers, and these were then used for sky subtraction, then this would explain the systematic shift in the vectors when comparing the results of Paper I and this work. It is not the specific bolometer used which affected the data, but how the Stokes' parameters were generated which led to the systematic shift. When POLPACK was used to generate Q and U , they were determined from a best fit to the predicted sinusoidal pattern, thus providing a much more sophisticated and robust means of extracting the polarization data. We are confident that the angles presented in this work are a correct representation of the polarization features in this region.

3. 850 μ m Polarization Data

3.1. A Non-Uniform Field across OMC-3

In Paper I, we presented maps of the distribution of position angle across four regions of OMC-3's filament. Based on Gaussian fits to those distributions, we showed that the position angles changed as one moved down the filament. In our re-reduced data set, shown in Figure 2, data are binned to $12''$ sampling and bad bolometers have been removed, thereby increasing the signal-to-noise in all regions. The only significant difference is the shift of the southern vectors to more negative angles as discussed in §2.

OMC-3 contains ten embedded cores as identified by Chini et al. (1997), some of which show evidence that protostellar collapse has already begun. However, the polarization pattern is not detected by the presence of the dense cores, but is continuous along the filament, as is also observed in the ridge of cores in the NGC 2024 region of Orion B (Matthews, Fiege & Moriarty-Schieven 2001). This could suggest that the cores, which have presumably

formed by the fragmentation of the filament, have preserved much of the highly ordered magnetic structure of the parent filament (Fiege & Pudritz 2000b). While this may be the case, it is also likely that, no matter what the field structure in the cores, the JCM T's 14⁰⁰ beam is insufficient to resolve it, since the polarization pattern we observe appears to be dominated by the larger filamentary structure.

It is possible to quantify our argument that the polarization pattern traces primarily the filament, rather than the dense cores embedded within it. The filament's axis was located by fitting a low order Chebyshev polynomial to the coordinates of the surface flux (or column) density maxima, equally spaced along the spine. A low order fit is desirable since the spine is then defined by a smooth curve which represents the global structure of the filament rather than responding in a noisy fashion to each small dense structure traced by dust. We then compared the orientation of each polarization vector with the local orientation of the filament. Orthogonal cuts at each position along the filament were made, and the position angle of the axis was compared to the position angles of polarization vectors lying along these radial cuts. Figure 3 presents histograms of the offset angles between polarization vectors and the filament orientation along its length. Along most of OMC-3, these distributions are centred on zero (although the FWHM are large). We fit Gaussians to these distributions and found mean offsets of 15°, 4° and 1° with σ of 26°, 21° and 29° for regions MM S1-4, MM S5-6 and the coreless-MM S7 regions respectively. South of MM S7, Figure 2 shows there is a shift in the vector orientation as the polarization pattern becomes increasingly misaligned with the fitted north-south spine of the filament. The distribution of offsets around MM S8 and MM S9 range from -60° to 90°. A Gaussian fit to this distribution yields a mean offset of 86°. So, these vectors are virtually perpendicular to the filament.

A side from the basic orientations of the polarization pattern discussed above, we note here that at the periphery of the detected polarization data, there are several locations in Figure 2 where the vectors appear to orient themselves along faint, extended dust structures. For example, south of MM S4 lie two small condensations of dust pointed southward. Note that the polarization data lie north-south in this region. Also, east of MM S6, a faint lane of dust extends to the north-east, toward the bright source at R.A. 05^h35^m29^s.9, DEC. 04°58'52".7 (J2000). The region surrounding MM S8 and MM S9 exhibits vector orientation aligned around 70° (east of north). This is where the filament appears widest in OMC-3, with bright peaks at the east (MM S10, Chini et al. (1997)) and west boundary of the polarization data. The suggestion of alignment of polarization vectors with extended faint dust lanes and the data presented in Figure 3 for the region from MM S1 to MM S7 provide strong support for a correlation between the polarization pattern and dense gas as traced by dust in that part of the filament.

3.2. Depolarization Along the Filament Spine

Diminished polarization percentage toward bright peaks is routinely observed in extended massive cores, such as those of OMC-1 at 100 and 350 m (Schleuning 1998) and even in interferometric maps of the protostellar source NGC 1333 IRAS4A (Girart et al. 1999). In Paper I we briefly discussed the depolarization observed for a perpendicular cut across MM S4. We can now generalize this result for the whole OMC-3 region. Figure 4 plots the polarization percentage of vectors with $p > 6$ versus the ratio of the intensity to the peak in the map where the intensities are estimated from the polarization data. This figure clearly shows that depolarization toward higher intensities is a general result in our data set. The same behavior is observed in three regions of Orion B (Matthews et al. 2001).

Examination of Figure 4 raises the question of whether the diminished polarization could be a systematic effect at low values of total intensity. The polarization percentage, p , is derived from the Stokes' parameters Q and U where $p = \frac{Q^2 + U^2}{I}$. When I is small and Q/I and U/I are even smaller, noise effects can lead to gross overestimates of p . Systematic effects can also be introduced by significant polarization in the chop position, or reference beam, of the observation, or in the bolometers selected for sky subtraction (see Appendix A).

Figure 5 shows the depolarization toward the filament axis for regions containing bright cores as well as the coreless region between MM S6 and MM S7. These plots are generated using lines perpendicular to the fitted slope of the OMC-3 filament discussed in §3.1. The polarization percentage versus (the magnitude of) the radial distance from the filament axis along these "radial cuts" are plotted. No interpolation is done; each plotted point is a true data point on Figure 2. Most of the cores (with the exception of MM S4) show increasing polarization at greater radial distances. The trend of declining polarization toward the axis is not limited to the bright cores embedded in the filament. Figure 5 shows that depolarization persists along the length of the filament spine, even in a region devoid of bright cores between MM S6 and MM S7. The depolarization becomes deeper as one moves southward, including the coreless region. The fact that depolarization is observed along the entire length of OMC-3 is further evidence that the polarization pattern is a feature of the filament itself and does not require the presence of dense, cold cores. Additionally, depolarization along the filament suggests that any model of the polarized emission from magnetized filamentary clouds must be able to explain the presence of depolarization toward the central axis.

Thus, we conclude that the depolarization effect is a feature of the filament, not the dense cores, although steeper depolarization may be observed near cores due to augmented effects of field tangling on scales smaller than the beam or more distinct grain changes. While the depolarization effect is a signature of a helical field, we do not suggest that field

geometry is the sole means by which such an effect could be produced. Other factors which can produce a depolarization hole include systematic effects (i.e. chopping onto polarized emission as discussed in Appendix A), although we do not think the flux levels in these maps could reproduce the depth of depolarization we observe. One possible explanation could be that the grain physics is changing with proximity to the axis of the filament, i.e. with density or optical depth (Hildebrand et al. 1999). If the degree of alignment or spin rate changes with density, then the grains near the central axis could exhibit a lesser degree of polarization. At higher column densities, the grains could become more spherical through agglomeration processes, thereby rendering them unpolarizable. If these changes are present at the densities and temperatures characteristic of the center of the filament, this too could explain, or at least contribute to, the depolarization effect.

3.3. Can Faraday Rotation Account for Depolarization?

Faraday rotation occurs if a linearly polarized wave encounters a plasma containing a magnetic field (i.e. the ISM). A linearly polarized wave can be decomposed into two circularly polarized waves of opposite orientations. These components propagate with different phase velocities in the plasma, if there is a component of the magnetic field along the line of sight. The net effect will be one of depolarization if the cloud is optically thin and field strength and electron densities are such that Faraday rotation is significant. Since thermal dust emission toward all molecular regions (with the exception of the central regions of dense collapsing cores) is optically thin, the net polarized emission measured by the telescope will be a sum over all emitting grains subject to different degrees of Faraday rotation depending on the different pathlengths through which they traveled through the cloud. Thus, vector addition of Faraday rotated emission from the far side of a cloud and virtually unaffected emission from the near side of the cloud could produce a net polarization vector of zero.

The plane of polarization of the linearly polarized wave rotates as it passes through the plasma by an amount:

$$\theta = RM \quad \text{radians} \quad (1)$$

where λ is the wavelength of the observation in meters and RM is the rotation measure, given by:

$$RM = (8.1 \times 10^5) \int n_e B_{\parallel} dr \quad \text{rad m}^{-2} \quad (2)$$

where B_{\parallel} is the magnetic field strength along the line of sight in Gauss; n_e is the number of electrons per cm^{-3} ; and dr is the path length in parsecs (Kraus 1986). Although we

cannot deduce a rotation measure from our data, it is useful to demonstrate that Faraday rotation has a negligible effect on the orientation of polarization vectors presented in Figure 2. The analysis can be broken into two parts: the possible effects of Faraday rotation in the ambient, diffuse ISM toward Orion; and within Orion A itself.

In the former case, we can derive B_{eff} at 850 μm by using the median value deduced from 81 extra-galactic sources at the high-longitude boundaries of the Canadian Galactic Plane Survey at 21 cm. For the vast majority of these sources, RM values between -400 and 50 rad m^{-2} have been measured, with a median value of 163 rad m^{-2} (Brown 2001). For $\lambda = 850$ μm , this RM implies an angular change of 1.2×10^4 rad or 0.007° of rotation along the whole line of sight through the Galaxy. Thus, any rotation effects of the ISM between the Sun and Orion, a mere 500 pc away, are negligible.

Within the Orion A cloud, an estimate of Faraday rotation is more difficult to deduce. Measurements have been made of the field strength toward the dense (10^6 cm^{-3}) CN core of OM C-1 of $B_{\text{eff}} = 0.36 \pm 0.08$ mG (Crutcher et al. 1999). Since the CN measurements sample gas up to 100 times denser than that sampled on large scales along OM C-3 at 850 μm , it is unlikely that the field strengths local to the gas sampled by our data would exceed 35 G at 10^4 cm^{-3} . Assuming an ionization fraction of 10^{-4} (i.e. Ungerechts et al. (1997)), implies that $n_e \approx 1 \text{ cm}^{-3}$ local to the gas sampled by the JCM T. At its widest point, the filament in OM C-3 is approximately $225''$ which corresponds to 0.5 pc. If its depth is of comparable scale, and if B_{eff} and n_e are assumed to be constant, equation (2) yields $\text{RM} = 14 \text{ rad m}^{-2}$ within the OM C-3 filament. Since the OM C-3 filament is clearly denser than the ambient molecular region around it, we assume it would be the strongest source of Faraday rotation, having higher n_e and B_{eff} values than its surroundings. Substitution in equation (1) yields $\theta = 6 \times 10^4$ degrees of rotation for the polarimetric angle through OM C-3. In regions denser than 10^4 cm^{-3} , rotation would be proportionally higher, although the depth (dr) of such regions would become progressively smaller. Hence we conclude that the effects of Faraday rotation cannot be responsible for the depolarization effect observed in OM C-3.

4. Interpreting the Polarization Pattern

As we concluded in Paper I, the re-reduction of data toward OM C-3 reveals no evidence for the presence of a uniform field on large scales across the filament since there are two distinct subsets of data { one aligned with and one orthogonal to the filament. Our analysis shows that along $\sim 75\%$ of the OM C-3's projected length, the polarization pattern follows the orientation of the filament, becoming misaligned only south of MM S7. Further analysis reveals that the depolarization effect toward OM C-3 is a global feature of the region, existing

along the entire length of the spine. Therefore, any theoretical models for this filament should support variations in field geometry and explain the depolarization effect in the absence of embedded cores.

In the far-infrared and submillimeter regimes, theoretical modelling of dust grains suggests that each grain along a line of sight contributes thermal radiation polarized perpendicular to the local direction of the magnetic field in the plane of the sky (Hildebrand 1988). As a result, polarimetry observations have often been interpreted by rotating the observed electric field vector orientations by 90° to estimate the magnetic field direction. However, since magnetic fields are inherently three dimensional, there may exist different configurations which can produce similar two dimensional polarization patterns. Since models of magnetized filamentary clouds are now available (Fiege & Pudritz 2000a; Carlqvist & Kristen 1997; Nakamura et al. 1993), a reasonable approach is to vary magnetic field parameters in a model and then generate the expected polarization pattern to compare to observations (Fiege & Pudritz 2000c). Note that the Fiege & Pudritz model employs an axisymmetric magnetic field, so that the field is helical in general. However, their model is also consistent with filaments threaded by purely poloidal fields, although such a geometry is not supported by this data set (see x5).

Some basic successes of the Fiege & Pudritz model include its prediction of an r^2 density profile for filaments, which has been observed in Orion A (Johnstone & Bally 1999) and two dark clouds in Cygnus (Alves et al. 1999; Lada et al. 1999). The model also predicts that the depolarization observed along the axis of the filament is a natural result of the helical field geometry and does not rely on poorly polarizing or poorly aligned grains at high optical depths although the field geometry certainly does not preclude the existence of such effects. The basic idea is that polarization contributions from the poloidally dominated axis of the filament partially cancel the contributions from the toroidally dominated envelope. The cancellation is greatest along the axis, creating the depolarization observed. However, we note that poorly polarizing or unaligned grains could act in concert with the helical field to amplify the depolarization.

The northern region of OMC-3 bears a strong resemblance to the inner regions of the Type 1 models of Fiege & Pudritz (2000c), for which $B_{z,s}/B_{\theta,s} = B_z/B_\theta$, the ratio of the poloidal to toroidal field components at the surface of the filament, ≈ 0.1 . Note that B_z/B_θ is at a minimum at the surface of the filament and is typically > 1 in the central regions. The models presented in Fiege & Pudritz (2000c) use a maximum polarization percentage of 10%, on the order of what we observe in OMC-3 and in three regions of Orion B (Matthews et al. 2001). Also, the width of the expected polarization hole predicted by the Fiege & Pudritz (2000c) model varies with $B_{z,s}/B_{\theta,s}$, increasing as a function of filament diameter

as the relative poloidal strength increases. According to these models, the ratio of the width of the polarization hole to the filament diameter should be 0.5 or less for Type 1 filaments. Therefore, more sensitive measurements with longer chop throws (or no chopping at all) should detect a decline in polarization percentage at larger radial distances from the filament, if there is no significantly magnetized medium external to the filament. The only region where this effect is suggested by our data is between MMS6 and MMS7. Figure 5c shows depolarization toward the axis and a single vector of declining polarization percentage at approximately 35° from the axis. Figure 2 shows that there are smaller polarizations below the $p = 6$ level, but these are not preferentially further from the filament than those of Figure 5c.

Polarization vectors perpendicular to the filament axis are predicted for poloidally dominated field patterns (see Fig. 1 of Fiege & Pudritz (2000c)). For filaments symmetric about a central axis, only vectors parallel or perpendicular to filament axes are expected (Fiege & Pudritz 2000c). Paper I reported a misalignment of the polarization vector position angles of $35^\circ - 47^\circ$ near MMS8 and MMS9 from the estimated filament orientation of 0° (east of north). Re-reduction and direct fitting of the filament spine yields a new estimate of 86° as the difference between the position angles of the vectors and the orientation of the filament in this region (see x 3.1). The fact that this misalignment occurs within the boundaries of a single SCUBA field of view raises concern that a systematic effect in observing technique could be producing these vectors. In Appendix A, it is shown that flux in the reference position can have detrimental effects on the measured polarization percentage and position angle. However, even in extreme cases of significant polarized flux in the reference position, errors of 90° in position angle can only be produced for observed intensities close to zero and are extremely unlikely unless the polarization percentage in the reference position exceeds that of the source. Thus, it is unlikely that this source of systematic error is responsible for the polarization angles observed.

Fiege & Pudritz (2000c) consider both toroidally and poloidally dominated field geometries. In the northern part of OMC-3, the alignment of the polarization vectors along the filament agrees well with the predictions for a toroidally dominated field geometry. However, a poloidally dominated field is expected to produce a polarization pattern offset by 90° in position angle from the filament axis. The poloidally dominated pattern thus predicts the position angles observed in the southern part of OMC-3. However, there are several marked differences between the predicted poloidally-dominated pattern and the observed vectors. The predicted pattern has a local maximum in polarization percentage along the axis, with two symmetric depolarization holes on either side (c.f. Fig. 1 of Fiege & Pudritz (2000c)). The polarization is then seen to rise again at larger radii from the axis. However, Figure 5b does not exhibit this behavior. The lowest values of polarization percentage measured are

along the axis, just as in the rest of OMC-3. The cores to the east and west and the widening of the filament here makes this area difficult to model. Further study of this portion of the OMC-3 region with a larger spatial scale map should provide more insight into the possibility that this region is poloidally, rather than toroidally, dominated.

Models invoking a purely poloidal magnetic field geometry aligned with the axis cannot be reconciled with the polarization pattern along the northern part of OMC-3. Additionally, an r^4 profile is predicted by the classic unmagnetized, isothermal filament of Ostriker (1964). In fact, it can be shown that all isothermal models limited to poloidal field geometries and constant flux-to-mass loading along the field lines produce density gradients steeper than r^4 . In the Integral-shaped Filament, Johnstone & Bally (1999) measure a profile of r^2 as predicted for a helical field geometry.

When the vectors are overlain on the total intensity maps generated from the polarization data (the sum of the maps obtained for each waveplate position), the extent of the maps is limited to the SCUBA fields observed with the polarimeter (c.f. Fig. 1 in Paper I). However, larger scale 850 μ m scan maps of this region (Johnstone & Bally 1999) allow us to place the polarization data in a broader context since they can be compared to larger scale dust features of the region. Close examination of the greyscale intensity of Figure 2 suggests two possible explanations for the observed 90° offset of the polarization vectors from the filament in the southern region of OMC-3. The dust emission becomes very extended and diffuse around MM S8-9. The continuum source MM S10 also lies to the east of the Integral-shaped Filament. A second (unnamed) peak could lie to the west of MM S8. These bright sources, coupled with the extended low intensity emission, suggest that a second filamentary structure, nearly orthogonal to the main filament, could be present. In this case, the polarization vectors are in fact aligned with a filament axis, but not that of the Integral-shaped Filament. Figure 6 shows a qualitative illustration of the effect of crossed filaments, both of which are threaded by helical fields. The second filament has half the central density of the main filament, which runs roughly north to south. The filaments intersect only in projection in this model; at the projected overlap, the vectors align with the second (east-west) filament. The Fiege & Pudritz (2000c) model defines three free parameters. The first is a concentration parameter, C , given by $C = \log(r/r_0)$ where r is the radius and r_0 is the core radius within which the density profile is flat. The core radius is given by $r_0 = (4/G\rho_c)^{0.5}$ where ρ_c is the one-dimensional line width, G is the gravitational constant and ρ_c is the central density. Both filaments have a concentration parameter, C , of 1.2, and dimensionless flux-to-mass loading parameters of $\lambda_z = 13$ and $\lambda_\phi = 18$ (as defined in Fiege & Pudritz (2000c)).

If a second filament is present, its effects on the polarization pattern should obviously

be limited to its width. This means that more extensive polarization observations south into OMC-2 should show re-alignment with the Integral-shaped Filament. The second filament also appears to extend in total intensity beyond the polarization data of Figure 2 to the northwest and southeast. Extended polarization data in these regions should reveal polarization data well-aligned with this faint dust emission, if two crossed filaments are present. Continued alignment with the dust structures will provide further evidence that the field orientation is related to the dense gaseous structures, either because the magnetic field has guided the condensation of gas, or because the gas has dragged in the magnetic field as the filament formed.

A second possibility is that the Integral-shaped Filament is the only filament present, but that it is bent (and thus changes inclination) south of MMS7. As discussed above, the northern region agrees well with the Type 1 models of Fiege & Pudritz (2000c) for a filament in the plane of the sky. However, even inclination of such models out of the plane of the sky is not expected to produce position angles other than 0 or 90° on the sky. If the filament were bent, however, then the cylindrical symmetry would be broken, and different position angles can result. This effect is easily considered qualitatively in terms of a wrapping cylindrical shape, such as a slinky, where the slinky represents magnetic field lines at a particular radius where the field is toroidally dominated. Consider what happens to the B loops when you bend the slinky: they are compressed on the inside of the bend and pulled apart on the outside. Due to concentration of the magnetic field, the inside part dominates, breaking the front-back symmetry in the straight filament models and causing the vectors to turn in the direction orthogonal to the field in the inner part of the bend. One can thus consider the effect on an observed polarization pattern in projection. As long as there is cylindrical symmetry, vectors in front of and behind the axis can be paired and will sum to either 0 or 90°. However, once bends are introduced, then the components of the vectors in the plane of the sky can be very different on either side of the filament axis, and the projected vectors cannot be paired. In this scenario, vector sums through the cloud may take on any value. Figure 7 shows an example of such a model, where we self-consistently bend both the filament and the helical field using a Lagrangian formulation of the induction equation in the limit of perfect MHD. A full description of our technique will be presented in a forthcoming publication. As for the crossed filament model discussed above, this model filament has a concentration parameter, C , of 1.2, and dimensionless flux-to-mass loading parameters of $z = 13$ and $\beta = 18$ (see Fiege & Pudritz (2000c)).

5. Discussion

We have re-reduced the Matthews & Wilson (2000) 850 μ m polarization data of the OM C-3 filament in Orion A, a region exhibiting strong filamentary structure and undergoing active star formation. Polarization observations are the key to revealing the presence of ordered magnetic fields in star-forming regions and determining whether their geometry is correlated with regions of high gas densities, as traced by dust. In OM C-3, we observe strong alignment between the polarization data and the orientation of the filamentary dense gas in the north, regardless of where embedded cores are located. Near the edges of our polarization data set, vectors appear to rotate to coincide with the orientations of faint structures of lower densities as illustrated in a larger scale intensity map of Johnstone & Bally (1999). Near the southern part of OM C-3, the vectors rapidly shift orientation, becoming almost orthogonal to the orientation of the bright Integral-shaped Filament, which could indicate the presence of a poloidally dominated field there.

Optical absorption polarization data on the periphery of the Lynds 1641 cloud (Vrba, Strom & Strom 1988) and in M 42 (Bregier 1976) reveal a net polarization direction of 120° . In the case of a uniform field, we would thus have expected emission polarization data to present vectors oriented at a position angle of $\sim 30^\circ$ (since absorption and emission polarimetry should be orthogonal if they trace the same field geometry). The 100 and 350 μ m data of OM C-1, located 20° further south along the Integral-shaped Filament from OM C-3, exhibit a polarization pattern with a mean direction of approximately 30° east of north (Schleuning 1998). These data were interpreted as support for a uniform field with position angle 120° (east of north) throughout the whole Orion A cloud. However, none of the vectors in OM C-3 suggest such a field geometry. Although the polarization data in the northern part of OM C-3 vary smoothly, they are not aligned with the data of OM C-1 nor the large scale optical data. In fact, the polarization orientations differ by 70° – 80° . Furthermore, the southern part of OM C-3 shows an abrupt change in polarization orientation, which is not easily explained by a uniform field. Changing vector orientations (i.e. south of MM S7) could indicate a bend in the field lines. This is why the polarization pattern from the OM C-1 core was interpreted as being pinched in due to collapsing gas (Schleuning 1998). The mean position angle near MM S8-9 is not consistent with that of either OM C-1 or northern OM C-3. If the magnetic field is uniform (i.e. of identical strength and direction throughout the depth of the cloud), all the vectors should line up in the same direction, regardless of the behavior of the gas.

Thus, taken as a whole, the data in OM C-3 alone are not consistent with a uniform field. Including the OM C-1 core data as well brings the number of "mean field directions" in these two data sets up to at least three. Under the picture of a uniform field, this should not be the case. Interestingly, the orientation of the filament in OM C-1 can be estimated

using the alignment of the two brightest cores. The angle between them is 30° east of north, which is consistent with the polarization position angles measured by Schleuning (1998) on large scales, but not with the interferometric position angles measured at 1.3 and 3.3 mm with the Berkeley Illinois Maryland Association (BIMA) interferometer (Rao et al. 1998).

An indirect method of estimating the magnetic field strength from polarimetry utilizes the assumption that the dispersion in the position angles of vectors is related to the magnetic field strength (Chandrasekhar & Fermi 1953). Inherent in this method is the assumption that there is a mean field orientation which can be identified (such as in the case of the spiral arms of the Galaxy in the original work of Chandrasekhar and Fermi). For complex field geometries in which the field reverses, there is no mean field to define; hence, we do not utilize this method to estimate a field strength toward OMC-3.

Our basic interpretations of the polarization pattern in Paper I remain unchanged. A comparison of filament to polarization position angles shows distributions centered on zero from MMS1 to MMS7, below which the vectors slowly rotate until they are misaligned from the filament (with a mean offset of $86^\circ \pm 19^\circ$). Additionally, the vector orientations are inconsistent with those predicted for poloidal fields where vectors would align perpendicular to the filament (Fiege & Pudritz 2000c). The northern data could suggest the presence of a transverse field. However, this interpretation would require either poorly aligned or poorly polarizing grains near the central axis of the filament. From a dynamical perspective, one might also expect a flattened sheet rather than a filament for this field geometry, since the magnetic support would be in a plane orthogonal to the field direction. Heiles (1987) observed Zeeman splitting of H I in the atomic envelope of Orion A and found evidence which supports the presence of a helical field geometry, although it was later interpreted in terms of the expanding Eridanus loop (Heiles 1997). The H I data sample a different gas component of the ISM than that probed by our polarimetry. Therefore, in order to interpret the three-dimensional field geometry local of the Integral-shaped Filament, it is vital that Zeeman splitting measurements of molecular gas within the filament be obtained.

In Paper I, we showed only a single radial cut across the MMS4 core to illustrate the depolarization across one of the filament's bright cores. A logarithmic plot of p vs. I for our entire data set shows that depolarization is a global feature in this filament. Furthermore, the distribution of the polarization percentage as a function of the distance from the filament spine reveals that depolarization exists along the entire length of OMC-3, most importantly across the coreless region between MMS6 and MMS7. This result implies that depolarization is a feature of this filament even in the absence of condensed cores. Therefore, any model of filamentary clouds must be able to explain this feature.

The existing polarization data toward OMC-3 are insufficient in spatial extent to dis-

criminate between two of our proposed explanations of a second filamentary structure or a bending in the Integral-shaped Filament. The behavior of the polarization south of MMS9 (into the region of OMC-2) is of particular interest. If the vectors in OMC-2 behave as the northern pattern of OMC-3, this could indicate support for a second filament, since only the region of juxtaposition is affected. (Observations of this region in CO with high velocity resolution will help to resolve the question of whether two filaments are juxtaposed on the sky.) On the other hand, if the vectors are asymmetric or misaligned from the parallel or perpendicular orientations in OMC-2, then this could indicate the model of a single bent filament better represents the physical properties of the Integral-shaped Filament. Extending the map to the east and west will reveal if strong polarization continues along the faint emission around MMS8 and MMS9. If neither hypothesis is supported by extending the data set, the filament may truly be poloidally dominated near the MMS8 and MMS9 cores.

In Paper I, we speculated that the effects of outflow from the powerful class 0 source MMS9 could have affected the magnetic field geometry to the east and west of that source, producing the polarization pattern observed. This is a particular concern for 850 μ m SCUBA polarimetry because the $^{12}\text{CO } J = 3 - 2$ line lies at the center of the 850 μ m filter bandwidth. The CO line may also be polarized and, if the CO emission is significant, it can dominate the polarization of the continuum. However, the only part of OMC-3 where the CO has been shown to dominate the 850 μ m continuum is in a Herbig-Haro knot west of the filament (Johnstone 2001).

Even if the field of an outflow is aligned with that of the young stellar object, it does not follow that the polarization directions would be the same. For example, Girart et al. (1999) found orthogonal polarization directions from 1.3 mm continuum dust in NGC 1333 IRAS 4A and $^{12}\text{CO } J = 2 - 1$ line in its outflow. Finally, the outflow of MMS9 does not extend as far north as MMS7, where the direction of the polarization vectors begins to change. New data on outflows in the OMC-2/3 region identify MMS9 as the primary driving source in the southern part of OMC-3, while MMS8 is not associated with outflow in either H_2 shocks or CO emission (Aso et al. 2000; Yu et al. 2000). The outflow from MMS9 is aligned in a northwest to southeast orientation, contrary to the northeast to southwest orientation of the continuum emission. Based on CO emission, Yu et al. (2000) claim that MMS10 as identified by Chini et al. (1997) has no submillimeter counterpart. However, in the 850 μ m map of Johnstone & Bally (1999) shown in Figure 1, there is a peak coincident with the 1.3 mm dust condensation observed previously. Aso et al. (2000) identify MMS10 as driving an east-west outflow. D disentangling the magnetic signatures of the cores and outflows in this region will require direct measurement of the polarization of the $^{12}\text{CO } J = 3 - 2$ or the $^{12}\text{CO } J = 2 - 1$ line.

We conclude that the helical field model of Fiege & Pudritz (2000a,c) is consistent with our observations. This model predicts the depolarization along the axis of filaments and the position angle patterns, as well as explaining the r^2 density profile observed by Johnstone & Bally (1999). Although a quantitative model of OMC-3 as a bent filament is not yet complete, we are actively pursuing this possibility as a promising explanation for our data. There is no reason to suppose that a filament extending over a parsec should maintain a single inclination relative to the plane of the sky. Conversely, the misalignment of vectors toward MM S8 and MM S9 may not be a misalignment at all if a second filament is juxtaposed on the Integral-shaped Filament at their positions. The current data set is not extensive enough to distinguish between these two possible filament-field geometries. Polarization mapping to the east, west and south of the current mapped area would provide more insight into the magnetic field geometry in this region. High resolution data are also needed to further investigate other sources of the depolarization effect along the axis of the filament.

The authors would like to thank J. Greaves, T. Jenness, and G. Moriarty-Schieven at the JCM T for their assistance with problems both large and small during and especially after observing. Thanks to D. Johnstone for making the 850 μ m scan map of the Integral-shaped Filament available to us and to J. Brown for access to the Faraday rotation data prior to its publication. We would also like to thank our referee for several suggestions which led to improvements in this manuscript. The research of BCM and CDW is supported through grants from the Natural Sciences and Engineering Research Council of Canada. BCM acknowledges funding from Ontario Graduate Scholarships. JDF acknowledges support from a postdoctoral fellowship, jointly funded by the Natural Sciences and Engineering Council and the Canadian Institute for Theoretical Astrophysics.

R E F E R E N C E S

- Aitken, D. K., Greaves, J. S., Crysostomou, A., Jenness, T., Holland, W. S., Hough, J. H.,
Pierce-Price, D., & Richer, J. 2000, *ApJ*, 534, 173
- Alves, J. F., Lada, C. J., & Lada, E. A. 1999, *ApJ*, 515, 265
- Aso, Y., Tatematsu, K., Sekimoto, Y., Nakano, T., Uemoto, T., Koyama, K., & Yamamoto,
S. 2000, *ApJS*, 131, 465
- Breger, M. 1976, *ApJ*, 204, 789
- Brown, J. C., 2001, PhD Thesis, in preparation
- Carlqvist, P., & Kristen, H. 1997, *A & A*, 324, 1115
- Chandrasekhar, S., & Fermi, E. 1953, *ApJ*, 118, 113
- Chini, R., Reipurth, B., Ward-Thompson, D., Bally, J., Nymann, L.-A., Sievers, A., &
Billawala, Y. 1997, *ApJ*, 474, L135
- Coppin, K. E. K., Greaves, J. S., Jenness, T., & Holland, W. S. 2000, *A & A*, 356, 1031
- Crutcher, R. M. 1999, *ApJ*, 520, 706
- Crutcher, R. M., Troland, T. H., Lazare, B., Paubert, G., & Kazes, I. 1999, *ApJ*, 514, L121
- Dotson, J. L., Davidson, J., Dowell, C. D., Schleuning, D. A., & Hildebrand, R. H. 2000,
ApJS, 128, 335
- Dowell, C. D. 2001, in preparation
- Dowell, C. D., Hildebrand, R. H., Schleuning, D. A., Vaillancourt, J., Dotson, J. L., Novak,
G., Renbarger, T., & Houde, M. 1998, *ApJ*, 504, 588
- Draine, B. T., & Weingartner, J. C. 1996, *ApJ*, 470, 551
- Fiege, J. D., & Henriksen, R. N. 1996, *MNRAS*, 281, 1038
- Fiege, J. D., & Pudritz, R. E. 2000a, *MNRAS*, 311, 85
- Fiege, J. D., & Pudritz, R. E. 2000b, *MNRAS*, 311, 105
- Fiege, J. D., & Pudritz, R. E. 2000c, *ApJ*, 544, 830
- Girart, J. M., Crutcher, R. M., & Rao, R. 1999, *ApJ*, 525, 109

- Greaves, J. S., Holland, W. S., & Ward-Thompson, D. 2001, *ApJ*, 546, L53
- Greaves, J. S., Holland, W. S., Jenness, T., Moriarty-Schieven, G., Chrysostomou, A., Berry, D. S., Murray, A. G., Nartallo, R., Ade, P. A. R., Gannaway, F., Haynes, C. V., Tamura, M., Mommose, M., & Morino, J.-I. 2001, *MNRAS*, submitted
- Greaves, J. S., Jenness, T., Chrysostomou, A. C., Holland, W. S., & Berry, D. S. 2000, in *Imaging at Radio through Submillimeter Wavelengths*, eds. J. G. Mangum & S. J. E. Radford, *ASP-C S* 217, 18
- Heiles, C. 1987, in *Interstellar Processes*, eds. Hollenbach, D. H., Thronson Jr, H. A. (Reidel), 171
- Heiles, C. 1997, *ApJS*, 111, 245
- Hildebrand, R. H., Davidson, J. A., Dotson, J. L., Novak, G., & Vaillancourt, J. E. 2000, *PASP*, 112, 1215
- Hildebrand, R. H., Dotson, J. L., Dowell, C. D., Schleuning, D. A., & Vaillancourt, J. E. 1999, *ApJ*, 516, 834
- Hildebrand, R. H. 1988, *QJRAS*, 29, 327
- Holland, W. S., Greaves, J. S., Ward-Thompson, D., & Andre, P. 1996, *A&A*, 309, 267
- Jenness, T., Lightfoot, J. F., & Holland, W. S. 1998, *Proc. SPIE*, 3357, 548
- Johnstone, D. 2001, private communication
- Johnstone, D., & Bally, J. 1999, *ApJ*, 510, L49
- Kraus, J. D. 1986. *Radio Astronomy*, (2d ed.)
- Lada, C., Alves, J., & Lada, E. 1999, *ApJ*, 512, 250
- Matthews, B. C., Fiege, J. D., & Moriarty-Schieven, G. H. 2001, in preparation
- Matthews, B. C., & Wilson, C. D. 2000, *ApJ*, 531, 868 (Paper I)
- Nakamura, F., Hanawa, T., & Nakano, T. 1993, *PASJ*, 45, 551
- Ostriker, J. 1964, *ApJ*, 140, 1056
- Pudritz, R. E. 1985, *ApJ*, 293, 216

- Puroell, E. M. 1979, *ApJ*, 231, 404
- Rao, R., Crutcher, R. M., Plambeck, R. L., & Wright, M. C. H. 1998, *ApJ*, 502, L75
- Schleuning, D. A. 1998, *ApJ*, 493, 811
- Schleuning, D. A., Dowell, C. D., Hildebrand, R. H., Platt, S. R., & Novak, G. 1997, *PASP*, 109, 307
- Shu, F. H., Adams, F. C., & Lizano, S. 1987, *ARA&A*, 25, 23
- Shu, F., Najita, J., Ostriker, E., Wilkin, F., Ruden, S., & Lizano, S. 1994, *ApJ*, 429, 781
- Uchida, Y., & Shibata, K. 1985, *PASJ*, 37, 515
- Ungerer, H., Bergin, E. A., Goldsmith, P. F., Irvine, W. M., Schloerb, F. P., & Snell, R. L. 1997, *ApJ*, 482, 245
- Vrba, F. J., Strom, S. E., & Strom, K. M. 1988, *AJ*, 96, 680
- Ward-Thompson, D., Kirk, J. M., Crutcher, R. M., Greaves, J. S., Holland, W. S., & Andre, P. 2000, *ApJ*, 537, 135
- Yu, K. C., Billawala, Y., Smith, M. D., Bally, J., & Butner, H. M. 2000, *AJ*, 120, 1974

A . Effects of a Polarized Reference (or Sky) Position

The quality of submillimeter polarimetry data can be strongly affected by chopping on and off the source during observing and sky noise removal in data reduction. The former can affect the results if the difference in intensity of the source minus chop is not actually zero, or if the chop positions, commonly called the reference positions, are significantly polarized. Sky removal requires one to select one or more SCUBA bolometers which are devoid of significant flux to estimate sky variations on the timescale of 1 s. If the flux in these bolometers is in fact polarized or non-zero, then polarization data for the whole data set could be affected.

Typically, in reducing polarimetry data, the assumption is made that fluxes in the chop and sky bolometer positions are negligible and unpolarized. These assumptions are most likely valid in the case of point-like sources (such as protostars) in non-clustered environments (such as Taurus or Bok globules) where the background, even if non-zero, is flat enough that chopping reduces the background effectively to zero. More typically in star-forming regions, however, bright cores may be embedded within more extended structures, and even the largest chop throws of 150–180'' (at the JCMT) may be insufficient to reach "empty", unpolarized sky. If one were only interested in cores, one could use small chops, removing significant amounts of extended flux, but even in such cases, the difference between the on-source and chop positions may not be zero at the edges of the array given the rapid declines in surface intensities. For example, 850 μ m data of the Integral-shaped Filament in which OMC-3 is located has been shown to exhibit a flux profile of r^{-1} , which implies a variation of flux across the filament on the scale of the chop throw (Johnstone & Bally 1999).

The effects of a polarized reference, or chop, position on the observed map are not necessarily intuitive. In order to illustrate the behavior of observed polarization percentage and position angle, we have used a simple model in which the polarization properties of the source and reference positions are known exactly. By subtracting the reference from the source polarization, the behavior of the observed polarization vectors can be compared to the input source values.

Linear polarization is defined by the Stokes parameters Q and U (and the total unpolarized intensity I),

$$Q = I_p \cos(2\psi) \quad U = I_p \sin(2\psi) \quad (\text{A1})$$

where I_p is the polarized intensity, the product of the polarization percentage, p , and the total intensity, I , and ψ is the polarization position angle. Note that under these definitions, Q and U execute a period in 180° instead of 360°. This reflects the reality that 180° offsets are not detectable in linear polarization.

The percentage polarization is defined by

$$p = \frac{p \sqrt{Q^2 + U^2}}{I} \quad 100\% \quad (\text{A } 2)$$

while the position angle is given by

$$= \frac{1}{2} \arctan \frac{U}{Q} \quad (\text{A } 3)$$

where $U=Q > 0$ for $180^\circ < 2\psi < 90^\circ$ and $0^\circ < 2\psi < 90^\circ$. A ratio of $U=Q < 0$ can be found only where $90^\circ < 2\psi < 0^\circ$ and $90^\circ < 2\psi < 180^\circ$. Finally, $U=Q = 0$ only where $2\psi = 0^\circ$ and $Q \neq 0$. Where both $Q = 0$ and $U = 0$ observationally, the source must be unpolarized.

If one defines I_s , p_s , and ψ_s values for a source and I_r , p_r , and ψ_r for a reference position, then one can deduce the quantities one would observe: I_{obs} , p_{obs} , and ψ_{obs} by simple subtraction of I , Q , and U values at the two positions. In this exercise, we do not include an estimate of the rms noise, which serves primarily to truncate the useful data set observed at low I , Q and U values. Additionally, although chopping is typically done to reference positions on either side of the source field, we will consider only the source data and one reference position.

SCUBA and other bolometric arrays (SHARC, BOLOCAM) sample a wide area of sky compared to previous single bolometer instruments. Thus, many flux levels may be present across their fields of view. One might suspect that during SCUBA observations (which allow a maximum chop throw of $3''$), the reference position could be so close spatially to the source position that the same polarization properties could be present at both positions. Smoothly varying polarization patterns have been observed in many star-forming regions (e.g. see Dotson et al. (2000)). Even in such cases, the observed polarization vector could be adversely affected; the magnitude of the effect depends on the relative polarized flux (i.e. p/I) between the source and reference fields.

One can consider two straightforward cases which illustrate the effects of chopping on the observed polarization vectors. In the first case, consider a source polarized at $\psi_s = 0^\circ$ and a reference polarization of $\psi_r = 90^\circ$. Using equation (A 1), the values of Q_s , U_s , Q_r , and U_r can be calculated in terms of the polarized intensities at each position: $I_{p;s}$ and $I_{p;r}$. Subtraction of the reference values of Q and U show that the observed quantity, U_{obs} , remains zero, so by equation (A 3), the position angle measured will be the same as that of the source. However, application of equation (A 2) yields the result

$$p_{\text{obs}} = p_s \frac{1 + (I_{p;r}=I_{p;s})}{1 - (I_r=I_s)}$$

where I_{obs} has been replaced by $I_s - I_r$. Therefore, the true p_s is recovered only if both $I_{pr}=I_{ps}$ and $I_r=I_s$ approach zero.

In the second case, consider a source polarized at $\theta_s = 0^\circ$ and a reference polarization with position angle $\theta_r = 45^\circ$. A similar calculation of respective Q and U values, subtraction and application of equations (A 3) and (A 2) reveals that since $U_{\text{obs}} \neq 0$, both the position angle and the percentage polarization will in this case differ from those of the source. The observed position angle is a function of $I_{pr}=I_{ps}$:

$$\theta_{\text{obs}} = \frac{1}{2} \arctan \frac{I_{pr}}{I_{ps}}$$

while the percentage polarization is again a function of $I_{pr}=I_{ps}$ and $I_r=I_s$:

$$p_{\text{obs}} = p_s \frac{1 + (I_{pr}=I_{ps})^2}{1 - (I_r=I_s)} :$$

In order to quantify this effect over many conditions, we subtracted a reference polarization from a source polarization under several different cases outlined in Table 2. In all cases, a source polarization of 10% and a position angle of 0° were used, with varying ranges of source intensity.² The reference polarization angle is assigned an offset from this value. The source total intensity is assigned a range of values from 1 to 20, and the reference flux is assumed to have a uniform polarized intensity equal to some fraction that of the source peak.

Figure 8 plots p_{obs} as a function of I_{obs} for Cases A, B and F. Where the reference polarization is aligned with the source polarization, the correct p_s is measured for all $I_{\text{obs}} > 0$ in Cases A and B. However, in Case F, the p_{obs} is underestimated, since $p_r > p_s$. For large offsets between θ_s and θ_r , the polarization percentage could be overestimated, particularly for low I_{obs} values. Near the source peak, the polarization observed converges on the true source polarization value. The values of $p_{\text{obs}}/p_s > 10$ are, in the case of $p_s = 10\%$, completely unphysical and would be disregarded in any data set. Positive or negative offsets in position angle between source and reference produce the same p_{obs} . For this reason, only the solutions for positive offsets have been plotted on Figure 8.

Figure 9 shows that θ_s is recovered in all three cases when the source and reference polarizations are aligned. When the source and reference polarizations are not aligned, more

²Calculations can be done with different θ_s values, but the results are completely identical to those presented here. What is relevant is the difference between θ_s and θ_r not the absolute value of either.

interesting results are obtained. The largest discrepancies in θ_{obs} occur when the differences between θ_s and θ_r are small. Figure 9 illustrates that, for high values of I_{obs} , the largest errors in θ_{obs} from θ_s are observed for $\theta_s - \theta_r = 45^\circ$, which corresponds to $2(\theta_s - \theta_r)$ of 90° . For very low I_{obs} , smaller offsets can produce an even larger error. As offsets increase toward 90° , a $2(\theta_s - \theta_r)$ value of 180° is approached. Since linear polarization measurements cannot discriminate between vectors 180° apart, the input θ_s is recovered. In Case A, which most closely parallels the MMS6 field of our data, at least in levels of intensity between the source and chop position (see x 2), the largest error which can be produced in position angle is 10° , and that is only for the lowest values of I_{obs} . In Case B, which has a source peak flux to reference flux ratio similar to that of the MMS8-9 region in the OMC-3 data set (based on the Johnstone & Bally (1999) scan map data), the most extreme errors in position angle predicted range from $(20^\circ - 30^\circ)$ even for very low intensities, as long as our assumption of similar polarization to the source holds. Even though we have noted that the largest errors in θ_{obs} occur for small angles, Figure 9 shows that in Case B, the small angle offsets do not dominate, and the θ_{obs} is within 20° of θ_s until fluxes are less than 10% of the peak I_{obs} . We have truncated our OMC-3 data set such that $I_{\text{obs}} > 0.0006$ (volts), which is approximately 10% of the faintest peak in our map (MMS7) with a flux of $0.00554 - 0.00002$ (volts). For still lower intensities (where I_{obs} approaches 0), the largest discrepancies from the input θ_s are no greater than 40° .

In comparison, Case F reveals potential errors of 90° for low $I_{\text{obs}} > 0$. If a true observation were done under these conditions, polarization vectors would be reliable only to a flux level about 50% of the observed peak. Near the peaks, errors are only on the order of $< 20^\circ$. Thus, even in this extreme case where the $p_r > p_s$ and the I_r is a significant fraction of I_s , it is unlikely that chopping alone could produce an alignment of θ_{obs} across a SCUBA field of view. In the idealized scenario we have discussed, the various fluxes across the SCUBA source field of view will be affected differently by the polarized flux in the reference position, creating vectors for which θ_{obs} varies systematically with I_{obs} . OMC-3's southern region contains vectors which are orthogonal to the filament orientation over the whole SCUBA field (a range of an order of magnitude in total flux). The vectors have a mean of 70° with a range up to 30° from that value. There is no systematic variation in position angle with intensity. We thus conclude that the simple scenario discussed here (a constant polarized flux at the reference position) cannot be responsible for the misalignment between the filament and polarization vectors. We cannot rule out a variable polarized flux across the SCUBA footprint at the reference position, but our examination of the Johnstone & Bally (1999) data does not reveal large variations in intensity at those positions. If polarization percentage were varying, we have no means of detecting this variation with our data set.

However, polarization has been detected at 350 μ m toward the northern part of OMC-3 using the Hertz polarimeter at the Caltech Submillimeter Observatory (Dowell 2001). These data show alignment along the filament as observed at 850 μ m with SCUBA, although the 350 μ m polarization percentages are $\sim 75\%$ those of the JCM T (Hildebrand et al. 2000). Since the CSO data were obtained with a chop throw of 6° (double that of the JCM T), and the behavior of the polarization pattern is consistent between the two instruments, this provides some re-assurance that the SCUBA position angle data have not been grossly affected by a significant polarized flux at the reference position.

In practice, efforts should be made to select reference positions which are devoid of significant flux compared to the flux levels in the source field of view. Figures 8 and 9 show that even if the polarization percentage is comparable in both fields, the effects on the observable quantities recovered are minimized greatly if the total flux levels are low at the reference position.

One of the key "observable" relationships in our data set of OMC-3 is the depolarization effect measured along the length of the filament. Systematically lower polarization percentages are measured toward regions of higher intensities. Figure 10 shows the $\log p_{\text{obs}}$ versus $\log (I_{\text{obs}}=I_{\text{obs,peak}})$ plots for six sets of θ between source and reference polarizations, which produces the largest error in polarization percentage. Unlike the OMC-3 data, for which the log-log plot of Figure 4 looks reasonably linear (given the noise and scatter), the depolarization effects of Figure 10 clearly are not linear. However, it is possible to sketch in a maximum and minimum slope. The minimum and maximum slopes encompass a range of slopes consistent with variation of percentage polarization with observed intensity for each of the six cases. Table 2 records the slopes; as one would expect, the depolarization produced is smallest for reference positions with low values of I_r and small values of p_r .

None of the slopes generated for data at high $I_{\text{obs}}=I_{\text{obs,peak}}$ reflect the slope of -0.65 derived for the OMC-3 data set. The closest effects are for reference fluxes $\sim 25\%$ of the flux peak, which we believe does not represent the observed conditions in any part of OMC-3. The slopes at high $I_{\text{obs}}=I_{\text{obs,peak}}$ are the most likely to be observed in real data, since they are exhibited where signal-to-noise will be high. However, at lower $I_{\text{obs}}=I_{\text{obs,peak}}$, steeper slopes could be produced, and for completeness, we have included these as maximum depolarization effects produced by each case. For all but the lowest reference flux considered (2% of the source peak), a slope of -0.65 could be explained by polarized flux in the reference position. We note, however, that these slopes are produced only in regions of low flux, whereas our data continue to exhibit this slope even at the highest flux values.

These calculations reveal that the effective "depolarization" created by chopping onto a polarized reference position is dependent on the intensity and degree of polarization present

as well as the offset between the source and reference position angle. We conclude that in the region of MMS8-9, it is possible that the depolarization observed could result from the scenarios described in Cases B, or possibly E. Cases C and F represent an extreme we do not believe exists in our data set. However, we note that the northern parts of OMC-3 have much lower reference fluxes compared to peak source positions (again, based on the Johnstone & Bally map). Near MMS6, for instance, the scenario is closer to Case A (or maybe Case D), for which the depolarization effect observed cannot be attributed to chopping effects.

B. Sky Subtraction

Bolometers must be carefully chosen for sky subtraction. Ideally, bolometers should be free of emission and, for polarimetry, unpolarized. SCUBA has a large field of view ($> 2.3^\circ$) and when observing point sources, there are typically many "empty" bolometers to choose from for sky subtraction. Extended sources prove more difficult.

Figure 11 compares the data obtained in 6 sets of 3 consecutive observations each toward the MMS8 and MMS9 region. Taking 3 consecutive scans of the same source allows the resultant maps to be quickly combined for increased signal-to-noise at the telescope and minimizes sky rotation between them. Sets 1 and 2 were obtained on 5 September; Sets 3-5 on 6 September; and Set 6 on 7 September. Before sky subtraction is performed, the polarization position angles appear highly uniform, but are not oriented in the same direction in each data set (see the left panels of Figure 11). For example, Set 1 exhibits vectors which align closely to the filament, while Set 3 appears just the opposite. However, the sky subtracted versions of each data set reveal very similar polarization patterns, although these generally appear messier than the unsubtracted data. Generally, in the sky subtracted maps, the overall orientation of the vectors is approximately east to west, although there is some high scatter in the lower signal-to-noise regions.

The uniformity in the non-sky subtracted frames is easily understood since the dominant factor in the polarization detected is due to sky. If the opacity of the sky is changing during a single observation (which it is, necessitating the removal of the sky's effects), then one can expect a very uniform polarization map. For instance, if the sky becomes steadily more opaque during an observation, then maps made at each successive position of the waveplate will contain fainter fluxes. When the waveplate positions are paired up and subtracted to deduce Q and U, then the results must be positive. If the sky is dominant, then Q and U will produce approximately the same fluxes, both positive, which yield a position angle of 45° (east of north). The removal of sky effects removes this uniformity and leaves the more structured polarization of the source itself. The uniformity of each subset once the sky has

been subtracted is a re-assurance that the subtraction routine is effectively removing sky variations.

C . Sub-dividing the OMC-3 data set

Figure 12 shows two subsets of the OMC-3 data. The constraints on the data plotted have been relaxed to reflect the fact that the noise is larger when only half the exposure time is used. Thus, instead of plotting values with the uncertainty in polarization percentage, $dp < 1\%$, we have plotted those vectors with $dp < 1.4\%$. Instead of selecting vectors with $p=dp = p_p > 6$, we have plotted those with $p_p > 4.2$.

The data reduction for each subset was performed in the same manner as for the entire data set as described in §2. Despite the fact that some data are missing from each set due to the removal of noisy bolometers, the polarization patterns shown in Figure 12 are very consistent with each other and with that of Figure 2. The alignment between filament and vectors in the north and misalignment in the south is observed in both maps. Depolarization toward the filament spine is also observed. Seventy percent of the polarization percentages of the 190 vectors in common between these two sets of data are not significantly different from one another (i.e. $\frac{(p_1 - p_2)}{(dp_1 + dp_2)} < 3$). The upper limit on the quantity $p_1 - p_2$ is estimated to be $dp_1 + dp_2$ because we have reason to suppose these errors will be correlated.

D . Polarization Percentages and Position Angles

Table 3 contains the percentage polarizations and position angles as plotted in Figure 2. The positions are given as arcsecond offsets from a position near the peak of MMS6, at J2000 coordinates $\alpha = 05^h 35^m 23^s.5$ and $\delta = 05^\circ 01' 32''.2$ ($\alpha = 05^h 32^m 55^s.6$ and $\delta = 05^\circ 03' 25''.0$ in B1950).

Table 1. Observing Parameters for Jiggly Mapping

Pointing Center		Chop Throw	Chop Position Angle	Number of
R.A. (J2000)	Dec. (J2000)	($^{\circ}$)	(east of north)	Times Observed
05 ^h 35 ^m 19 ^s 3	05 00 ^o 36 ^m 9	150	30	6
05 ^h 35 ^m 18 ^s 2	05 00 ^o 21 ^m 8	150	30	17
05 ^h 35 ^m 23 ^s 5	05 01 ^o 32 ^m 2	150	100	6
05 ^h 35 ^m 26 ^s 5	05 03 ^o 57 ^m 4	150	100	9
05 ^h 35 ^m 27 ^s 5	05 03 ^o 32 ^m 5	150	90	9
05 ^h 35 ^m 26 ^s 5	05 05 ^o 31 ^m 4	150	65	8
05 ^h 35 ^m 27 ^s 5	05 05 ^o 21 ^m 5	150	65	14

Table 2. Systematic Depolarization Created by Chopping onto Polarized Sky

Case	I_r	p_r	Slope of $\lg p_{\text{obs}}$ vs. $\lg I_{\text{obs}}$ at $s_r = 90$	
			minimum (high I_{obs})	maximum (low I_{obs})
A	0.4 (2% source peak)	10%	0.085	0.39
B	2 (10% source peak)	10%	0.28	0.65
C	5 (25% source peak)	10%	0.50	0.81
D	0.4 (2% source peak)	20%	0.085	0.49
E	2 (10% source peak)	20%	0.34	0.76
F	5 (25% source peak)	20%	0.56	0.88

Table 3. OMC-3 850 m Polarization Data

R A . (^h)	DEC . (^m)	p (%)	dp (%)	p	()	d ()
48:0	304:5	8.93	0.85	10.5	88:3	2.7
60:0	292:5	13.03	0.78	16.6	78:5	1.7
48:0	292:5	10.83	0.47	23.0	86:5	1.2
36:0	292:5	13.92	0.61	22.7	89:7	1.3
60:0	280:5	12.44	0.62	20.2	75:5	1.4
48:0	280:5	5.01	0.33	15.3	89:0	1.9
36:0	280:5	10.02	0.39	25.6	87:7	1.1
24:0	280:5	13.28	0.60	22.1	84:7	1.3
12:0	280:5	12.53	0.77	16.2	85:3	1.8
0:0	280:5	8.18	0.69	11.9	65:9	2.4
12:0	280:5	7.92	0.92	8.6	70:2	3.3
108:0	268:5	7.36	0.39	18.8	73:6	1.5
96:0	268:5	6.94	0.43	16.1	65:5	1.8
84:0	268:5	16.76	0.75	22.2	71:3	1.3
72:0	268:5	2.66	0.62	4.3	68:4	6.7
60:0	268:5	4.33	0.36	11.9	66:9	2.4
48:0	268:5	2.80	0.18	15.5	79:3	1.8
36:0	268:5	5.73	0.25	23.0	79:2	1.2
24:0	268:5	9.01	0.40	22.6	85:2	1.3
12:0	268:5	6.22	0.42	14.8	87:3	1.9
0:0	268:5	4.63	0.54	8.6	79:7	3.3
12:0	268:5	9.46	0.70	13.5	77:9	2.1
120:0	256:5	2.61	0.37	7.0	43:3	4.1
108:0	256:5	4.93	0.29	16.8	54:2	1.7
96:0	256:5	8.87	0.41	21.8	62:7	1.3
84:0	256:5	15.87	0.77	20.7	78:1	1.4
72:0	256:5	4.84	0.63	7.7	69:2	3.7
60:0	256:5	4.49	0.25	18.3	71:4	1.6
48:0	256:5	2.60	0.15	17.5	68:7	1.6
36:0	256:5	2.09	0.19	11.1	71:8	2.6

Table 3 | Continued

R A . (^h)	DEC . (^m)	p (%)	dp (%)	p	()	d ()
24:0	256:5	2.00	0.34	5.8	85:6	4.9
12:0	256:5	8.01	0.36	22.3	79:8	1.3
0:0	256:5	7.70	0.43	17.9	77:2	1.6
12:0	256:5	3.80	0.73	5.2	67:6	5.5
132:0	244:5	6.15	0.44	13.9	74:3	2.1
120:0	244:5	10.43	0.35	29.4	72:6	1.0
108:0	244:5	8.13	0.43	18.9	73:9	1.5
96:0	244:5	14.15	0.64	22.1	81:4	1.3
84:0	244:5	15.15	0.76	19.8	85:5	1.4
72:0	244:5	12.76	0.47	27.4	77:0	1.0
60:0	244:5	3.29	0.20	16.8	63:2	1.7
48:0	244:5	1.59	0.11	14.3	60:3	2.0
36:0	244:5	2.18	0.15	14.7	59:6	2.0
24:0	244:5	2.93	0.29	10.2	70:9	2.8
12:0	244:5	1.41	0.30	4.6	62:5	6.2
0:0	244:5	10.02	0.42	24.0	80:8	1.2
12:0	244:5	11.51	0.79	14.6	87:1	2.0
132:0	232:5	7.02	0.43	16.5	51:2	1.7
120:0	232:5	8.95	0.43	20.8	66:3	1.4
108:0	232:5	6.29	0.57	11.1	64:4	2.6
96:0	232:5	13.09	0.67	19.5	69:2	1.5
84:0	232:5	10.59	0.57	18.6	63:6	1.5
72:0	232:5	6.77	0.35	19.1	72:7	1.5
60:0	232:5	3.71	0.18	20.6	60:1	1.4
48:0	232:5	2.58	0.10	26.3	64:3	1.1
36:0	232:5	3.02	0.13	22.4	68:9	1.3
24:0	232:5	4.41	0.24	18.1	68:4	1.6
12:0	232:5	5.78	0.29	20.1	60:1	1.4
0:0	232:5	4.01	0.42	9.7	88:2	3.0
12:0	232:5	6.22	0.61	10.1	48:0	2.8

Table 3 | Continued

R A . (^h)	DEC . (^m)	p (%)	dp (%)	p	()	d ()
24:0	232:5	10.85	0.83	13.0	51:5	2.2
132:0	220:5	6.35	0.77	8.2	48:8	3.5
120:0	220:5	6.95	0.80	8.7	81:0	3.3
108:0	220:5	4.97	0.71	7.0	53:9	4.1
96:0	220:5	9.44	0.72	13.0	59:0	2.2
84:0	220:5	4.64	0.46	10.0	74:2	2.9
72:0	220:5	4.90	0.30	16.4	63:6	1.7
60:0	220:5	4.47	0.17	26.4	64:1	1.1
48:0	220:5	1.50	0.09	16.2	61:4	1.8
36:0	220:5	2.82	0.15	18.7	64:6	1.5
24:0	220:5	4.44	0.39	11.4	53:1	2.5
12:0	220:5	5.70	0.55	10.4	68:4	2.8
0:0	220:5	4.87	0.40	12.1	76:0	2.4
12:0	220:5	7.13	0.48	14.9	72:8	1.9
24:0	220:5	8.37	0.76	10.9	59:8	2.6
96:0	208:5	3.18	0.90	3.5	55:8	8.1
84:0	208:5	6.67	0.46	14.6	62:7	2.0
72:0	208:5	4.09	0.25	16.1	75:2	1.8
60:0	208:5	2.61	0.15	17.3	63:5	1.7
48:0	208:5	2.42	0.12	20.3	64:2	1.4
36:0	208:5	4.46	0.22	20.3	68:5	1.4
24:0	208:5	10.29	0.57	18.2	66:8	1.6
12:0	208:5	5.06	0.82	6.2	73:2	4.6
0:0	208:5	8.26	0.44	18.6	61:5	1.5
12:0	208:5	10.23	0.55	18.6	61:2	1.5
96:0	196:5	8.72	0.79	11.1	52:5	2.6
84:0	196:5	4.97	0.62	8.0	72:9	3.6
72:0	196:5	3.25	0.33	9.7	72:5	2.9
60:0	196:5	2.53	0.22	11.5	57:6	2.5
48:0	196:5	2.88	0.23	12.4	59:8	2.3

Table 3 | Continued

R A . (^h)	DEC . (^m)	p (%)	dp (%)	p	()	d ()
36:0	196:5	5.01	0.46	10.9	81:3	2.6
0:0	196:5	16.91	0.68	24.8	70:5	1.2
12:0	196:5	15.73	0.73	21.6	57:5	1.3
72:0	184:5	8.80	0.92	9.6	79:4	3.0
60:0	184:5	3.46	0.43	8.0	71:8	3.6
48:0	184:5	6.78	0.47	14.4	66:6	2.0
36:0	184:5	14.11	0.92	15.3	79:6	1.9
60:0	172:5	8.09	0.55	14.8	71:8	1.9
48:0	172:5	4.89	0.43	11.4	50:7	2.5
60:0	160:5	8.68	0.47	18.4	56:6	1.6
48:0	160:5	5.51	0.29	19.3	60:4	1.5
36:0	160:5	4.77	0.41	11.7	53:5	2.4
108:0	148:5	5.74	0.92	6.2	22:3	4.6
60:0	148:5	3.21	0.36	9.0	16:2	3.2
48:0	148:5	2.03	0.17	11.8	21:4	2.4
36:0	148:5	2.94	0.25	11.6	38:5	2.5
24:0	148:5	2.32	0.76	3.1	41:5	9.4
108:0	136:5	2.33	0.78	3.0	55:8	9.6
96:0	136:5	5.13	0.69	7.5	37:7	3.8
84:0	136:5	5.02	0.65	7.8	44:2	3.7
72:0	136:5	2.24	0.40	5.5	25:6	5.2
24:0	136:5	3.18	0.46	7.0	37:7	4.1
96:0	124:5	4.55	0.87	5.2	5:7	5.5
84:0	124:5	1.88	0.53	3.5	25:3	8.1
72:0	124:5	2.16	0.27	8.0	0:2	3.6
60:0	124:5	2.85	0.17	16.5	6:4	1.7
48:0	124:5	2.01	0.14	14.0	14:8	2.0
36:0	124:5	1.69	0.19	8.8	17:9	3.3
12:0	124:5	7.35	0.56	13.2	9:2	2.2
96:0	112:5	4.39	0.92	4.8	49:0	6.0

Table 3 | Continued

R A . (^o)	DEC . (^o)	p (%)	dp (%)	p	()	d ()
84:0	112:5	4.15	0.58	7.2	25:6	4.0
72:0	112:5	2.75	0.31	8.9	6:3	3.2
60:0	112:5	1.81	0.24	7.5	2:8	3.8
48:0	112:5	1.77	0.20	9.0	17:4	3.2
36:0	112:5	1.77	0.25	7.1	19:9	4.1
24:0	112:5	1.49	0.50	3.0	76:6	9.6
12:0	112:5	2.53	0.49	5.1	35:8	5.6
0:0	112:5	4.34	0.74	5.9	20:1	4.9
96:0	100:5	3.31	0.85	3.9	50:8	7.4
84:0	100:5	4.19	0.70	6.0	16:8	4.8
72:0	100:5	8.22	0.63	13.1	12:9	2.2
48:0	100:5	3.23	0.30	10.8	34:7	2.7
36:0	100:5	1.95	0.32	6.1	26:8	4.7
24:0	100:5	3.65	0.79	4.6	58:0	6.2
12:0	100:5	11.23	0.95	11.9	71:7	2.4
48:0	88:5	2.14	0.49	4.3	15:7	6.6
36:0	88:5	1.98	0.32	6.2	45:7	4.6
24:0	88:5	3.78	0.45	8.4	16:5	3.4
12:0	88:5	3.22	0.75	4.3	53:0	6.6
48:0	76:5	7.98	0.64	12.4	31:6	2.3
36:0	76:5	4.00	0.34	11.9	35:2	2.4
12:0	76:5	5.99	0.76	7.9	13:5	3.6
48:0	64:5	7.59	0.86	8.9	2:7	3.2
36:0	64:5	2.00	0.33	6.1	23:3	4.7
24:0	64:5	2.35	0.33	7.1	30:1	4.0
12:0	64:5	4.88	0.65	7.5	0:5	3.8
12:0	52:5	5.53	0.52	10.6	4:2	2.7
36:0	40:5	7.18	0.69	10.4	0:5	2.8
24:0	40:5	2.86	0.48	6.0	39:3	4.8
36:0	28:5	5.59	0.81	6.9	3:1	4.1

Table 3 | Continued

R A . (^h)	DEC . (^m)	p (%)	dp (%)	p	()	d ()
24:0	28:5	2.23	0.52	4.3	40:8	6.7
12:0	28:5	1.00	0.32	3.1	32:1	9.2
0:0	28:5	3.46	0.37	9.3	41:3	3.1
12:0	28:5	9.02	0.73	12.3	44:9	2.3
48:0	28:5	8.33	0.62	13.4	37:0	2.1
60:0	28:5	8.43	0.68	12.3	20:9	2.3
36:0	16:5	6.90	0.66	10.5	24:7	2.7
24:0	16:5	2.43	0.50	4.8	9:2	5.9
0:0	16:5	1.71	0.23	7.5	26:5	3.8
12:0	16:5	4.08	0.37	10.9	3:5	2.6
24:0	16:5	4.40	0.88	5.0	0:4	5.7
36:0	16:5	3.93	0.71	5.5	41:2	5.2
48:0	16:5	1.48	0.36	4.2	33:0	6.9
72:0	16:5	5.11	0.48	10.7	14:1	2.7
84:0	16:5	8.94	0.81	11.0	39:5	2.6
12:0	4:5	1.72	0.27	6.3	33:8	4.5
0:0	4:5	1.81	0.16	11.4	41:8	2.5
12:0	4:5	1.57	0.28	5.5	10:1	5.2
24:0	4:5	4.00	0.32	12.5	19:9	2.3
36:0	4:5	2.77	0.33	8.5	26:7	3.4
48:0	4:5	1.23	0.25	5.0	19:0	5.7
60:0	4:5	1.42	0.32	4.4	5:3	6.5
72:0	4:5	3.13	0.28	11.4	14:4	2.5
84:0	4:5	2.23	0.39	5.8	17:2	5.0
96:0	4:5	11.17	0.77	14.5	13:8	2.0
36:0	7:5	5.73	0.98	5.9	33:0	4.9
24:0	7:5	2.46	0.62	4.0	41:0	7.2
12:0	7:5	2.67	0.32	8.3	24:1	3.5
0:0	7:5	1.11	0.12	9.0	35:6	3.2
12:0	7:5	2.75	0.12	23.1	31:3	1.2

Table 3 | Continued

R A . (^o)	DEC . (^o)	p (%)	dp (%)	p	()	d ()
24:0	7:5	3.75	0.19	19.7	28:5	1.5
36:0	7:5	3.12	0.22	13.9	30:9	2.1
48:0	7:5	2.59	0.23	11.3	45:8	2.5
60:0	7:5	3.41	0.29	11.7	3:7	2.4
72:0	7:5	2.28	0.28	8.1	16:8	3.5
84:0	7:5	3.50	0.38	9.3	21:0	3.1
96:0	7:5	3.96	0.53	7.5	1:7	3.8
12:0	19:5	5.13	0.39	13.3	0:8	2.2
0:0	19:5	4.05	0.17	23.5	29:3	1.2
12:0	19:5	3.63	0.10	37.1	32:7	0.8
24:0	19:5	4.14	0.11	39.1	42:1	0.7
36:0	19:5	3.72	0.17	21.6	45:1	1.3
48:0	19:5	3.40	0.18	18.9	60:3	1.5
60:0	19:5	1.45	0.21	6.8	64:8	4.2
72:0	19:5	2.34	0.25	9.3	17:7	3.1
84:0	19:5	3.68	0.38	9.6	0:3	3.0
96:0	19:5	3.17	0.43	7.3	23:5	3.9
108:0	19:5	6.48	0.63	10.3	14:7	2.8
12:0	31:5	6.73	0.85	8.0	4:5	3.6
0:0	31:5	7.10	0.30	23.3	18:0	1.2
12:0	31:5	5.05	0.13	39.8	31:0	0.7
24:0	31:5	2.72	0.10	27.0	40:7	1.1
36:0	31:5	2.01	0.08	23.7	50:6	1.2
48:0	31:5	1.58	0.09	18.1	51:7	1.6
72:0	31:5	1.83	0.17	10.8	24:8	2.6
84:0	31:5	2.39	0.25	9.5	25:3	3.0
96:0	31:5	5.13	0.35	14.8	28:6	1.9
108:0	31:5	7.79	0.52	14.9	18:6	1.9
120:0	31:5	8.56	0.72	11.9	12:9	2.4
0:0	43:5	12.83	0.57	22.6	8:7	1.3

Table 3 | Continued

R A . (^o)	DEC . (^o)	p (%)	dp (%)	p	()	d ()
12:0	43:5	5.16	0.23	22.4	29:7	1.3
24:0	43:5	3.39	0.15	22.1	46:3	1.3
36:0	43:5	2.04	0.09	23.3	51:8	1.2
48:0	43:5	1.82	0.07	27.5	54:1	1.0
60:0	43:5	1.88	0.07	28.4	45:8	1.0
72:0	43:5	2.16	0.09	24.0	33:0	1.2
84:0	43:5	3.05	0.13	23.0	34:4	1.2
96:0	43:5	2.05	0.24	8.5	32:6	3.4
108:0	43:5	4.89	0.38	12.8	85:7	2.2
120:0	43:5	6.92	0.47	14.9	24:1	1.9
132:0	43:5	2.88	0.66	4.4	43:2	6.5
12:0	55:5	5.51	0.43	12.9	21:2	2.2
24:0	55:5	2.54	0.21	12.0	54:6	2.4
36:0	55:5	2.45	0.13	18.5	44:0	1.5
48:0	55:5	2.12	0.09	23.5	48:4	1.2
60:0	55:5	2.15	0.07	29.0	46:5	1.0
72:0	55:5	2.32	0.07	33.7	43:9	0.8
84:0	55:5	3.06	0.10	31.2	38:8	0.9
96:0	55:5	2.12	0.15	14.5	25:0	2.0
108:0	55:5	2.66	0.30	8.8	27:9	3.3
120:0	55:5	3.34	0.34	9.7	38:8	2.9
132:0	55:5	2.75	0.52	5.3	17:8	5.4
24:0	67:5	2.75	0.38	7.2	52:8	4.0
36:0	67:5	2.52	0.23	11.1	57:2	2.6
48:0	67:5	2.75	0.14	19.2	44:6	1.5
60:0	67:5	2.85	0.10	28.3	51:0	1.0
72:0	67:5	2.60	0.06	40.9	46:3	0.7
84:0	67:5	2.32	0.08	29.2	34:5	1.0
96:0	67:5	2.72	0.13	20.5	45:7	1.4
108:0	67:5	2.36	0.24	9.9	18:2	2.9

Table 3 | Continued

R A . (^o)	DEC . (^o)	p (%)	dp (%)	p	()	d ()
120:0	67:5	2.45	0.37	6.7	89:1	4.3
132:0	67:5	3.01	0.44	6.9	4:1	4.2
144:0	67:5	4.33	0.56	7.8	15:2	3.7
36:0	79:5	3.78	0.30	12.6	43:4	2.3
48:0	79:5	3.23	0.20	16.3	49:9	1.8
60:0	79:5	3.70	0.15	24.5	54:7	1.2
72:0	79:5	3.54	0.10	35.2	52:4	0.8
84:0	79:5	2.31	0.11	21.8	55:3	1.3
96:0	79:5	2.50	0.14	17.8	50:9	1.6
108:0	79:5	1.48	0.22	6.6	27:8	4.3
120:0	79:5	3.18	0.33	9.6	13:9	3.0
132:0	79:5	3.52	0.36	9.7	19:5	2.9
144:0	79:5	4.01	0.59	6.8	17:6	4.2
36:0	91:5	7.85	0.55	14.3	33:9	2.0
48:0	91:5	5.37	0.35	15.5	53:0	1.8
60:0	91:5	5.59	0.21	26.4	52:3	1.1
72:0	91:5	5.22	0.20	26.6	51:5	1.1
84:0	91:5	5.14	0.17	30.8	47:1	0.9
96:0	91:5	4.52	0.23	19.8	49:6	1.4
108:0	91:5	1.87	0.25	7.3	38:3	3.9
120:0	91:5	2.93	0.25	11.9	23:9	2.4
132:0	91:5	3.30	0.26	12.6	6:4	2.3
144:0	91:5	7.69	0.60	12.9	10:0	2.2
48:0	103:5	12.31	0.98	12.5	68:5	2.3
60:0	103:5	6.95	0.45	15.4	46:7	1.9
72:0	103:5	6.64	0.29	22.8	45:1	1.3
84:0	103:5	5.15	0.27	19.1	62:3	1.5
96:0	103:5	3.50	0.38	9.3	36:7	3.1
108:0	103:5	2.50	0.33	7.6	18:5	3.8
120:0	103:5	1.97	0.22	9.1	38:6	3.2

Fig. 1. Comparison of position angle distributions in the MMS8-9 region. We show the distribution of position angles for the southern part of the OMC-3 map as presented in Paper I (distribution A) and this work (distribution B). Distribution A can be fit by two Gaussians of means 33° and 47° (with standard deviations of 5° and 15° respectively). Distribution B can be fit by two Gaussians of means 63° and 82° (with standard deviations of 7° and 9° respectively). The vectors are on average shifted by 30° by the improved data reduction techniques of POLPACK. The effect is restricted to the MMS-9 region.

Fig. 2. $850\ \mu\text{m}$ polarization pattern across OMC-3. A portion of the $850\ \mu\text{m}$ intensity map of Johnstone & Bally (1999) is shown in colored greyscale. The greyscale range is 1.5 to 3.5. The polarization mapping covers only a portion of the area shown. Polarization data were sampled at $3''$ and have been binned to $12''$ (slightly less than the JCMT $850\ \mu\text{m}$ beam width of $14''$). The polarization vectors plotted all have percentage polarization $> 1\%$, an uncertainty in polarization percentage $< 1\%$ and a total intensity three times that of the sky bolometer level and $\sim 10\%$ of the faintest peak, MMS7. The thinnest vectors have a signal-to-noise in polarization percentage, $p_p > 3$, while the medium thickness vectors have $p_p > 6$. Most vectors are bold and have $p_p > 10$. These vectors are accurate in position angle to better than 10° , 4.8° and 2.9° , respectively. The central region of MMS7 and the region south of MMS6 are devoid of vectors since the polarization percentages there are less than 1% . The mean polarization percentage of the plotted vectors is 5.0% in 286 vectors. The coordinates of the map are J2000.

Fig. 3. The relative angles between the filament orientation and the position angles of polarization vectors (with $p_p > 6$) along radial cuts to the filament are shown for four regions of the OMC-3 map. Only vectors with $p_p > 6$ are used. The filament orientation is derived from a cubic spline fit to the intensity of OMC-3. For three of the four subregions, the offsets are centered around zero. For the region around MMS8 and MMS9, a Gaussian fit to this profile yields a mean and standard deviation of $94^\circ \pm 19^\circ$.

Fig. 4. A logarithmic plot of polarization percentage versus intensity (scaled by the maximum intensity point) reveals that higher intensities have systematically lower polarizations. Values plotted are those on Figure 2 which have $p_p > 6$. The decreasing trend cannot be accounted for by the uncertainties shown here. A χ^2 power law fit of the form $p = A I^{-\alpha}$ yields the A and α parameters recorded on the log-log plot. A slope of 0.65 effectively characterizes these data.

Fig. 5. Plots showing the polarization percentages as a function of radial distance from the filament axis toward different regions of OMC-3. Depolarization is exhibited toward the filament axis in all cases. Panels (a) and (b) show data around all six distinguishable cores.

Table 3 | Continued

R A . (^h)	DEC . (^m)	p (%)	dp (%)	p	()	d ()
132:0	103:5	3.55	0.21	16.8	24:7	1.7
144:0	103:5	5.90	0.59	10.0	16:9	2.9
60:0	115:5	4.20	0.77	5.5	42:0	5.3
72:0	115:5	6.35	0.44	14.5	48:1	2.0
84:0	115:5	6.91	0.39	17.9	52:8	1.6
96:0	115:5	4.45	0.55	8.0	38:5	3.6
108:0	115:5	2.98	0.47	6.4	50:6	4.5
120:0	115:5	3.90	0.22	17.8	27:3	1.6
132:0	115:5	4.37	0.28	15.4	9:0	1.9
72:0	127:5	6.26	0.72	8.6	45:4	3.3
84:0	127:5	8.35	0.55	15.3	43:4	1.9
96:0	127:5	4.39	0.53	8.3	10:6	3.5
108:0	127:5	1.85	0.50	3.7	19:9	7.8
120:0	127:5	5.48	0.42	13.0	46:6	2.2
132:0	127:5	5.77	0.80	7.2	61:8	4.0
96:0	139:5	3.82	0.89	4.3	3:6	6.7

Panel (c) shows the coreless region between M M S6 and M M S7. The depolarization effect is particularly strong for M M S8 and M M S9. Only vectors with $p_p > 6$ are used.

Fig. 6. | A qualitative model of the polarization pattern produced by a crossing of two filaments threaded by helical magnetic fields. The second (roughly east-west) filament has only half the central density of the main filament, which is meant to represent the Integral-shaped Filament. Both filaments lie in the plane of the sky. The model has been convolved with a Gaussian where the beam size is one fifth the filament diameter. Vectors shown have $p > 0.05p_{\text{max}}$ and $I > 0.05I_{\text{max}}$ where $p_{\text{max}} = 10\%$.

Fig. 7. | A qualitative model of the polarization pattern produced by a magnetized filamentary cloud where the southern half of the filament has been bent into an arc with a radius of curvature of 6.4 times the filament's diameter. The whole filament is inclined to the plane of the sky at an angle of 20° and then rotated in the plane of the sky by 225° . The model is convolved with the same Gaussian beam as Figure 6, and the constraints on the vectors displayed are identical. The bending of the filament breaks the symmetry of the models presented in Fiege & Pudritz (2000c) causing the polarization pattern from the inner region of the bend to dominate, as discussed in the text.

Fig. 8. | Ratio of observed to source polarization percentage versus observed intensity as a function of the observed peak intensity for three of the cases identified in Table 2. In each case, the source is polarized at a level of 10% . The ratios of input parameters of polarization percentage and intensity at the reference position compared to those at the source position are smallest for Case A and largest for Case F. The offset between source and reference angles, $\theta_s - \theta_r$, are labelled in each case. Clearly, the systematic effects due to chopping become more significant as the polarized flux in the reference beam grows relative to that of the source.

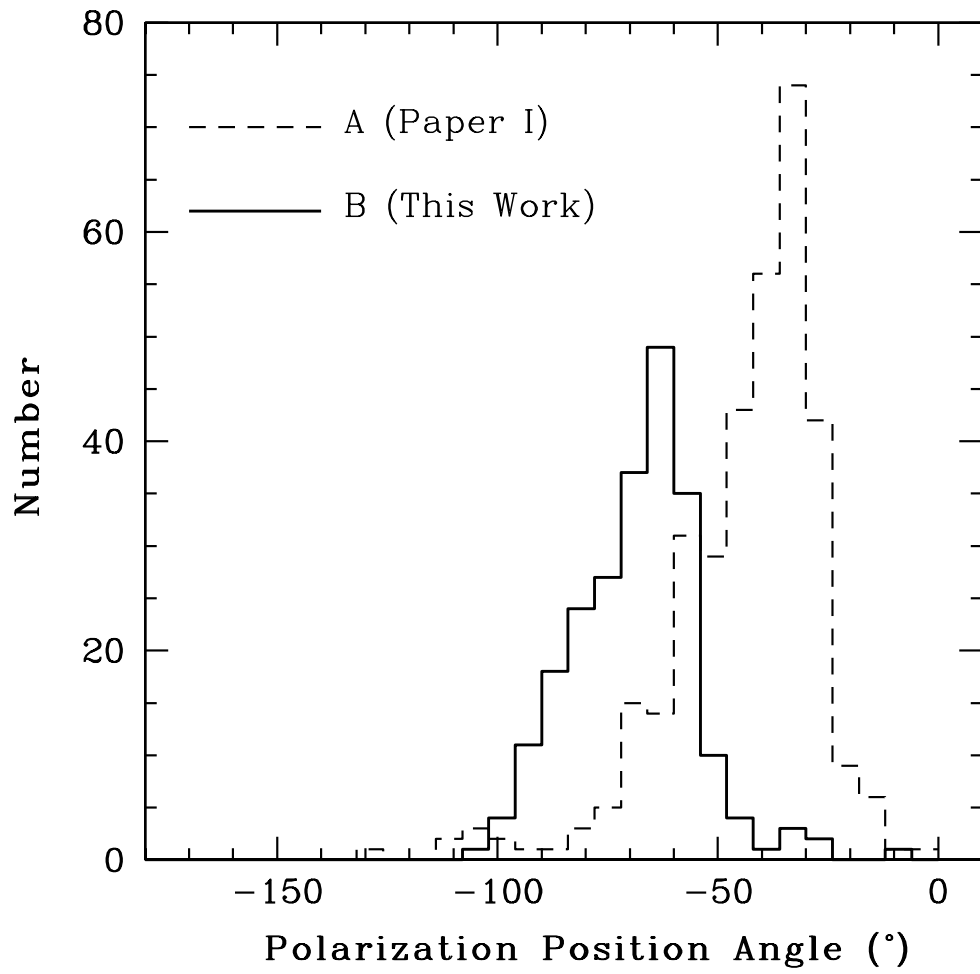
Fig. 9. | Observed position angles at various observed intensities (as a function of the observed flux peak) for Cases A, B and F as described in Table 2. The assigned position angle of the source was 0° . Solutions for positive and negative offsets between source and reference position angles are symmetric about the source position angle; hence, we show only solutions for positive offsets here. The solution for an offset of 90° is discussed in the text and is identical to the solution for 0° . The offset angles, $\theta_s - \theta_r$, are labelled in each case. As for percentage polarization in Figure 8, the lower the ratio of total flux in the reference position to the source, the less impact chopping has on the observed values at the source position.

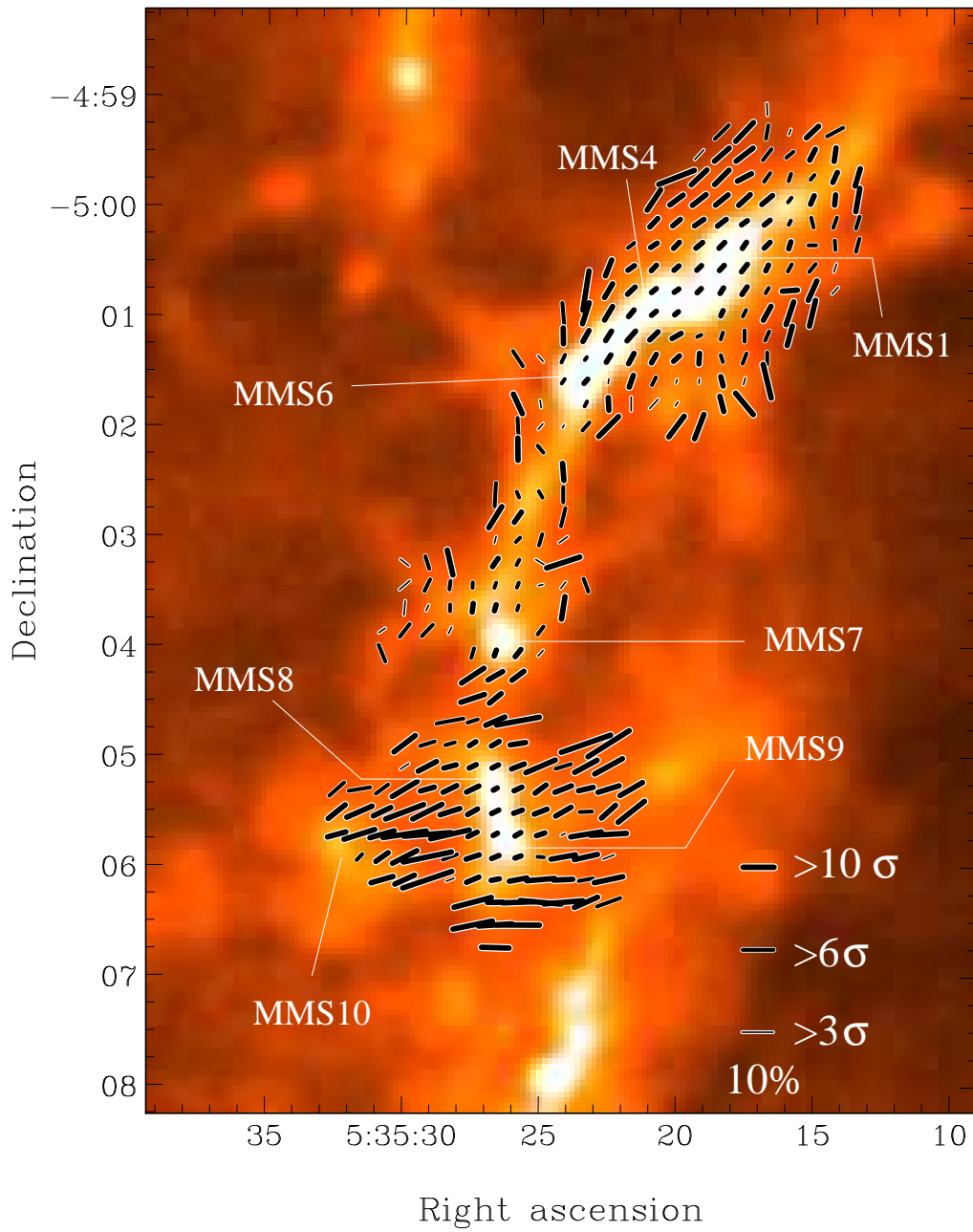
Fig. 10. | Depolarization effects expected for the cases described in Table 2. As Figure 4 shows, decreased polarization percentage with increased intensity is a global feature in

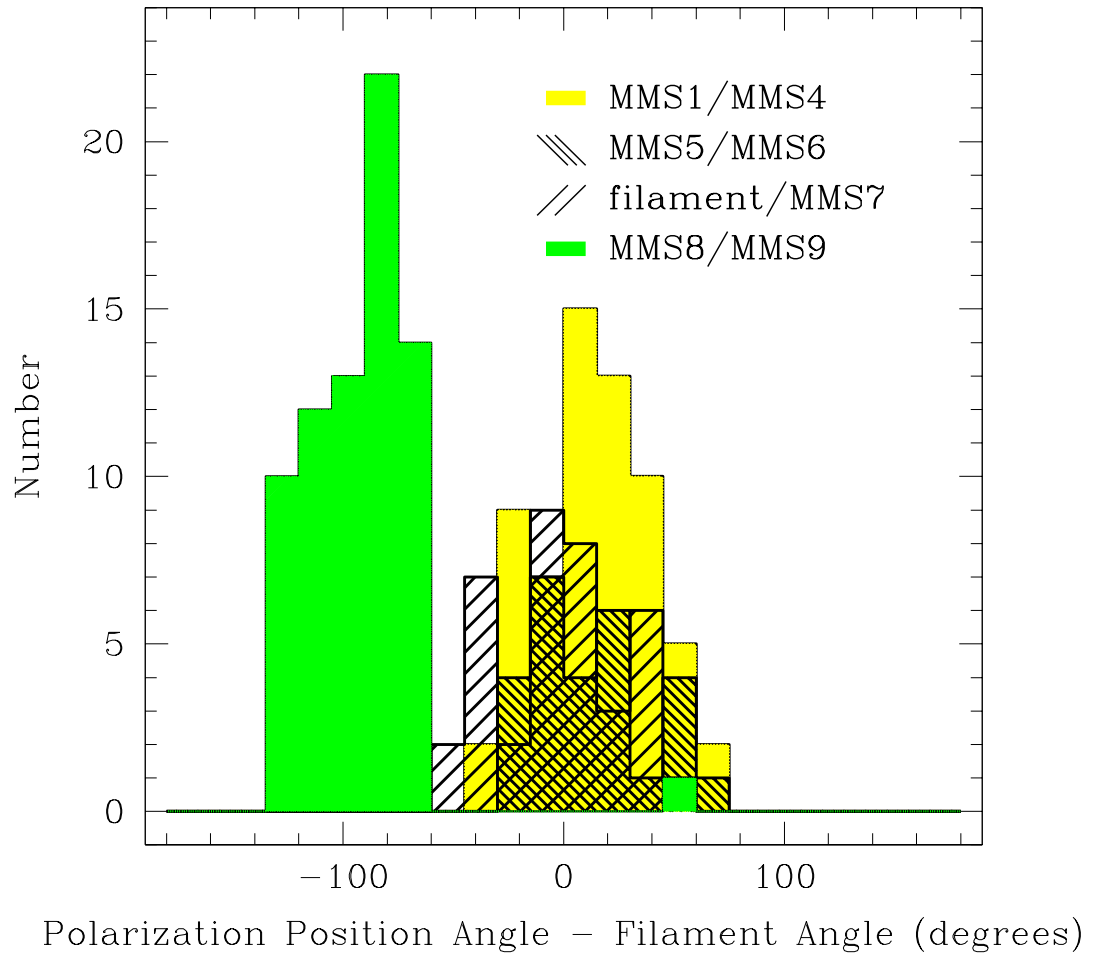
OM C-3. Such an effect can clearly be produced by chopping onto a reference position with significant polarization, although the magnitude of the slope produced diminishes as the flux of the reference position (with respect to the source) decreases.

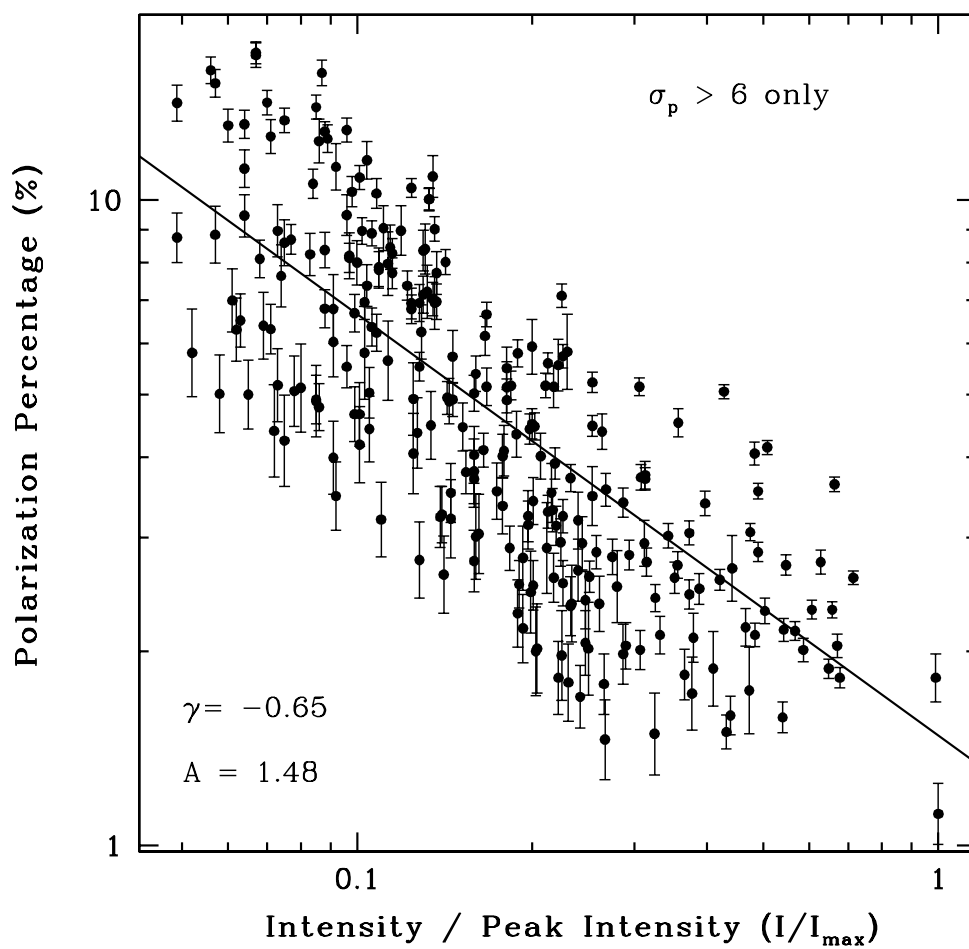
Fig. 11. Six data sets of the MM S8-MM S9 region are shown, each reduced with (right) and without (left) sky subtraction. These maps reveal that a high degree of uniformity in position angle can be observed before sky subtraction is performed. These patterns can be created by variations in sky conditions during the 12 minute polarization cycle and must be removed to reveal the true polarization vectors of the source.

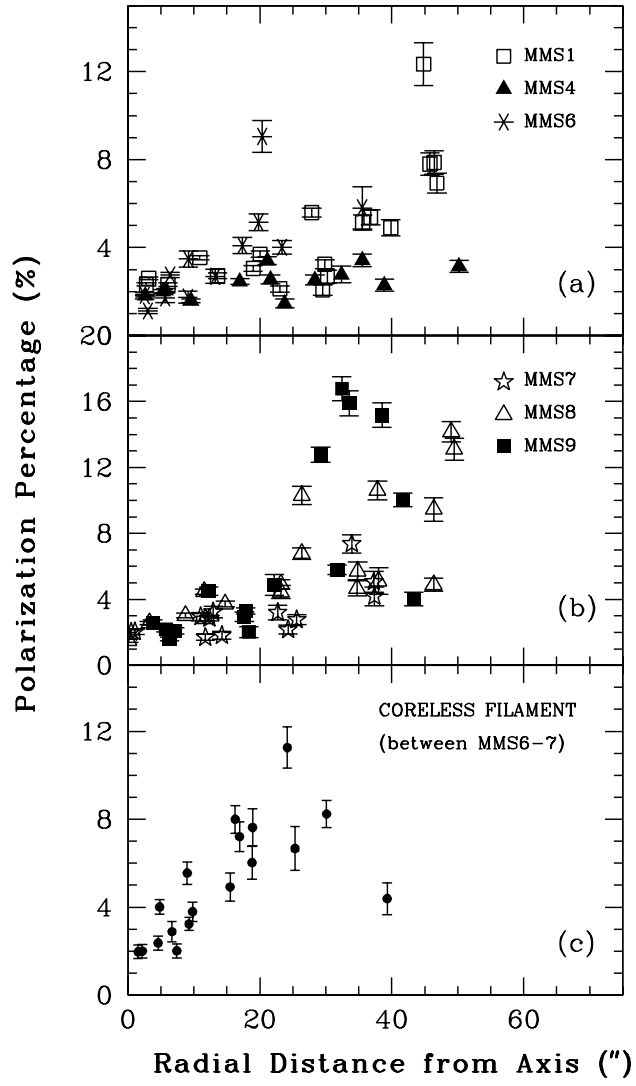
Fig. 12. These two figures illustrate the consistency between two halves of the OM C-3 data set. Polarization vectors plotted have $p > 1\%$, an uncertainty in polarization percentage, dp , $< 1.4\%$ and $p=dp > 4.2$.



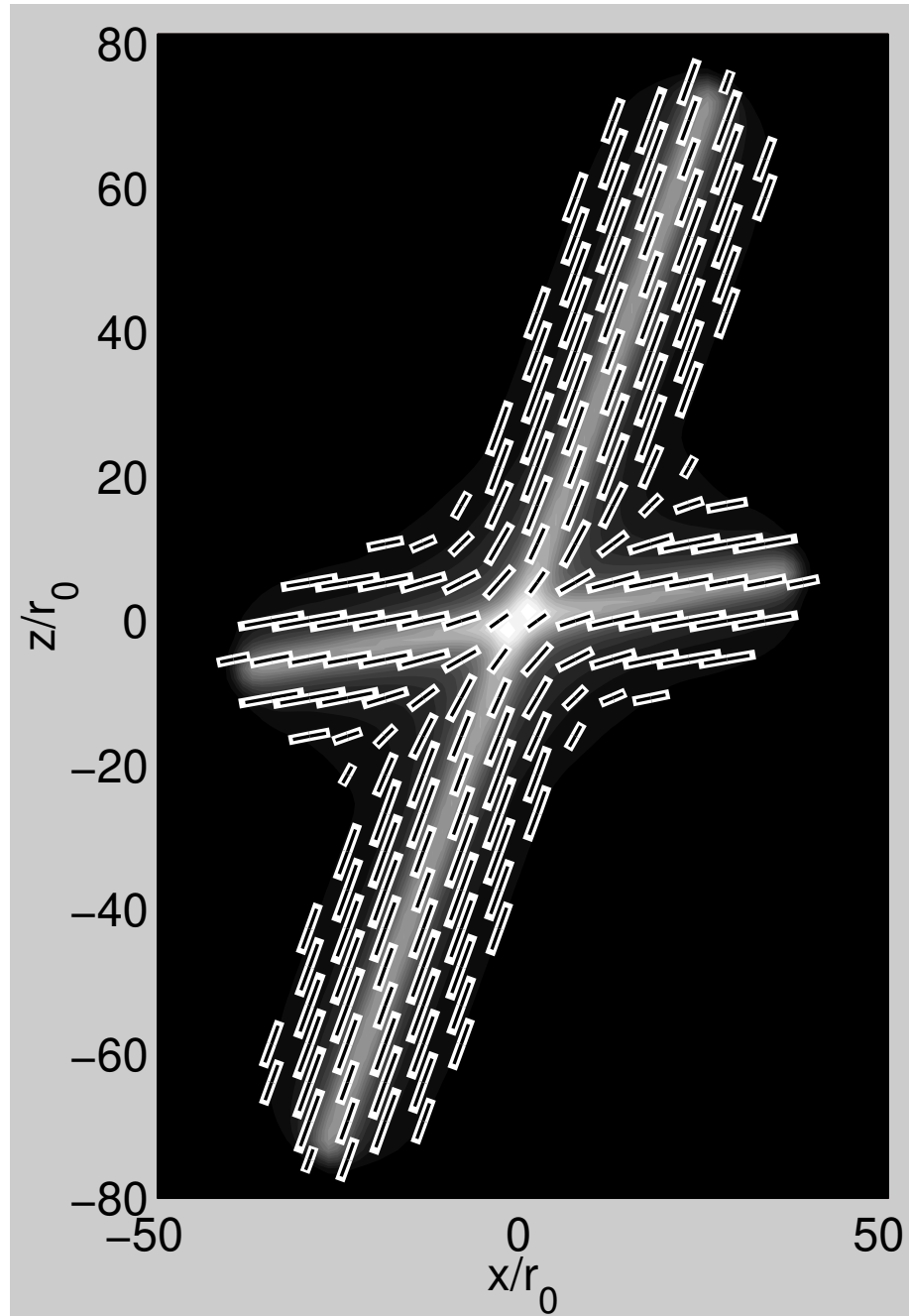


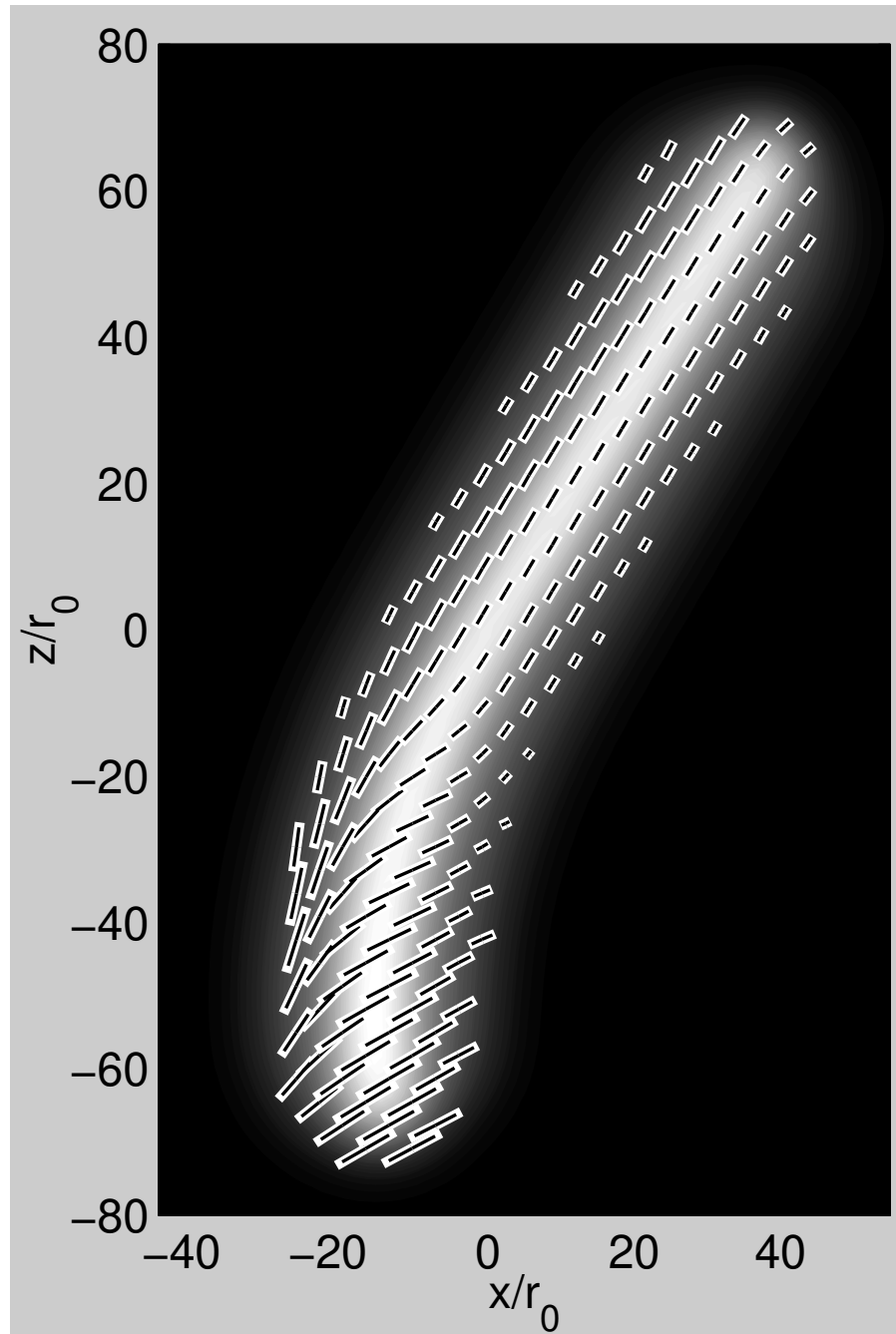


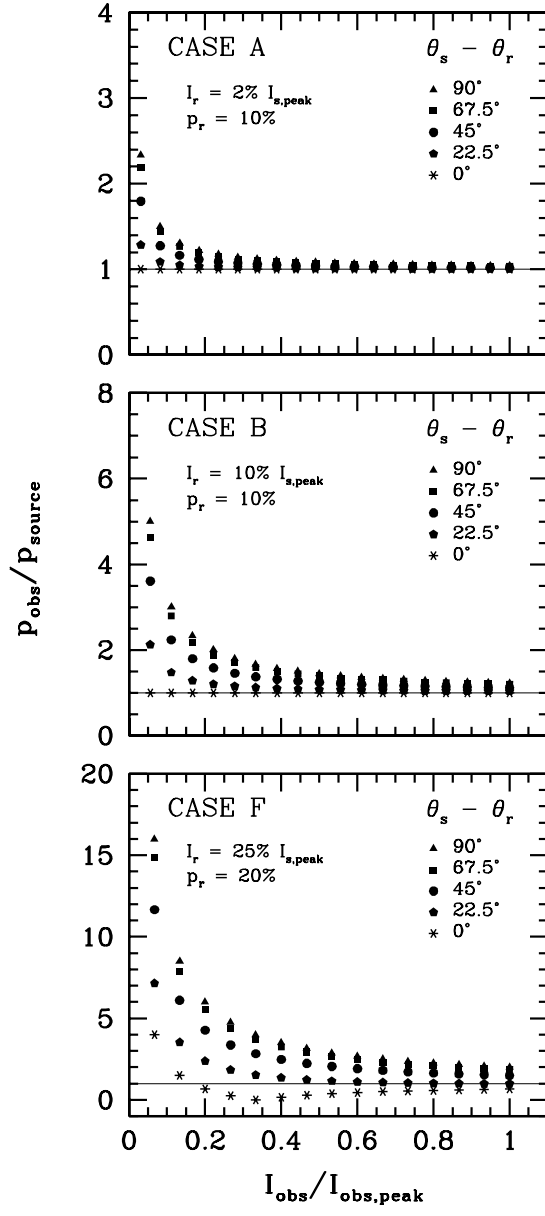


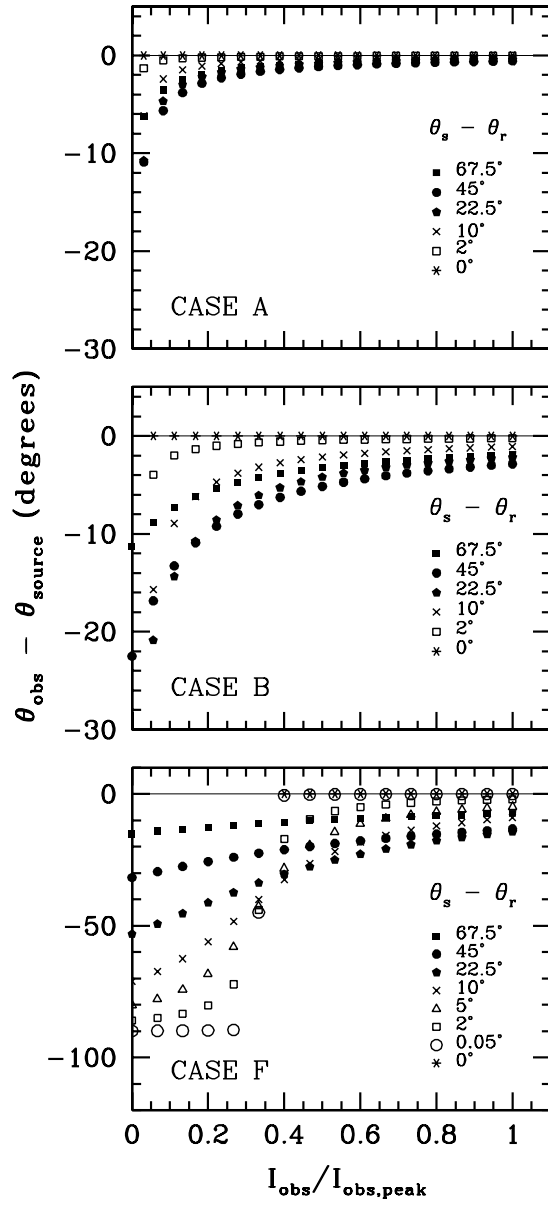


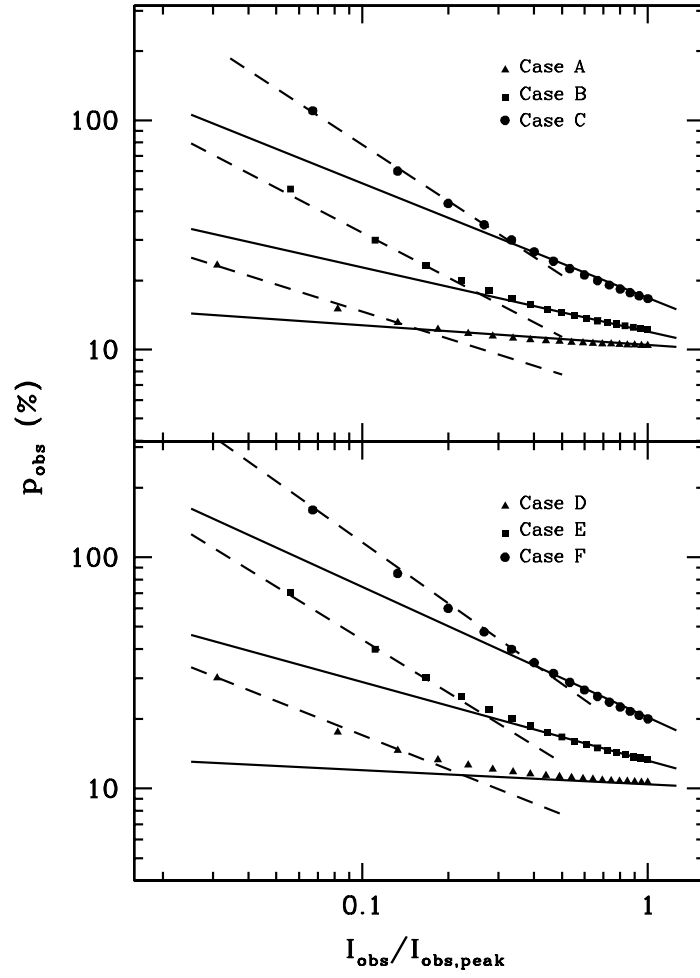
{ 50 {

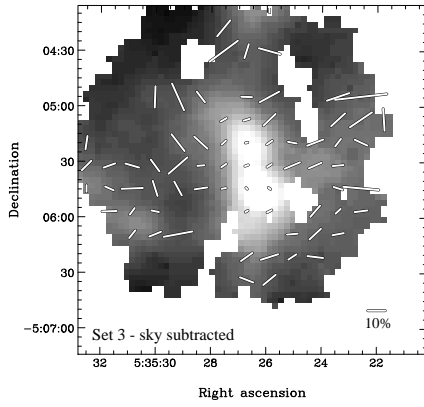
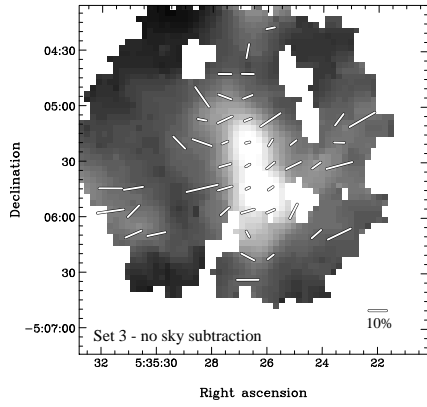
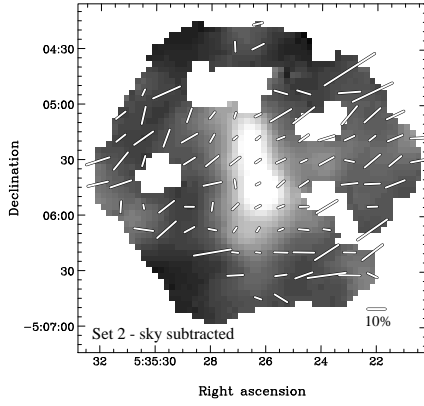
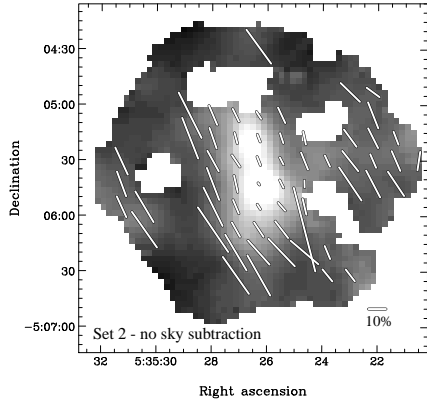
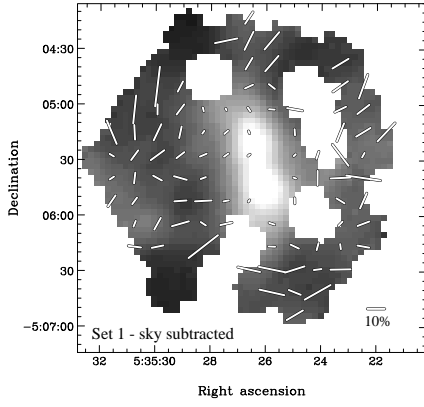
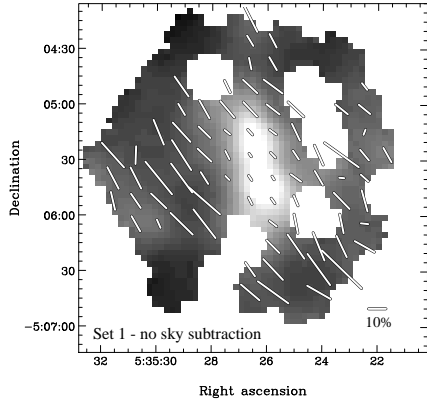


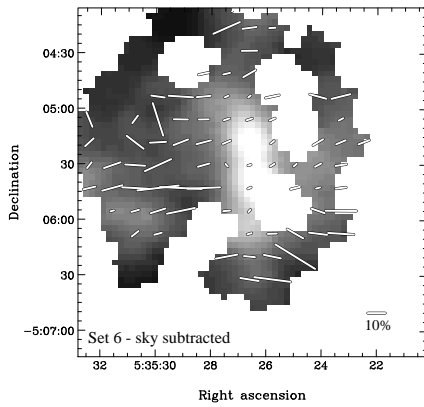
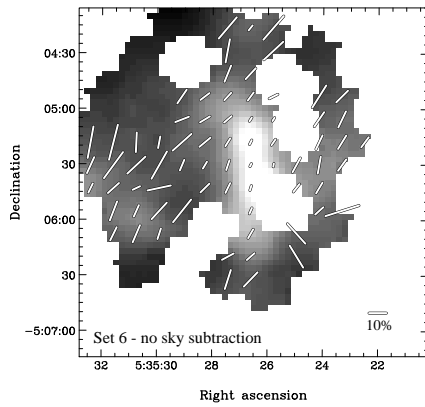
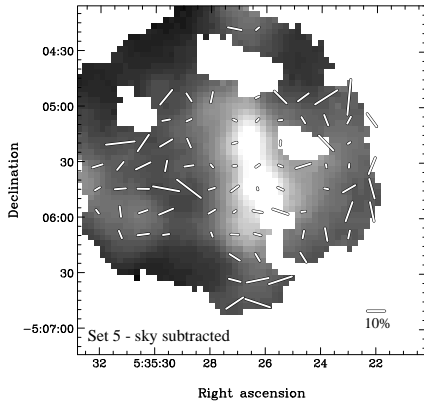
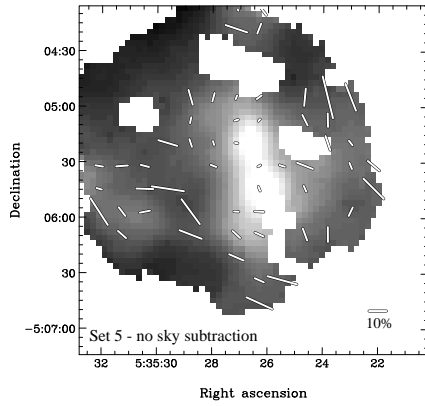
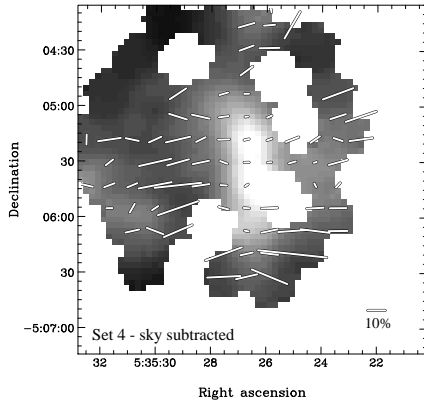
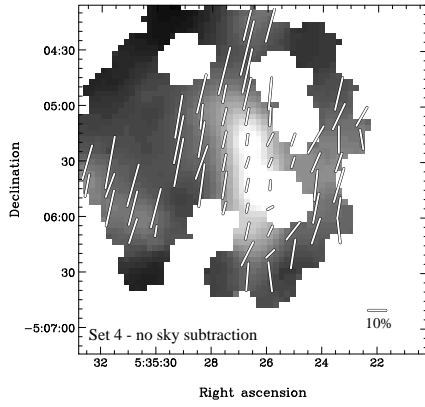


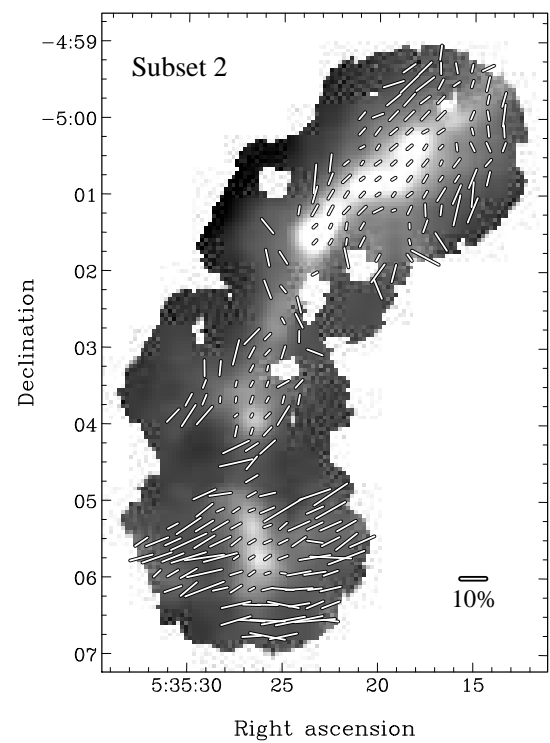
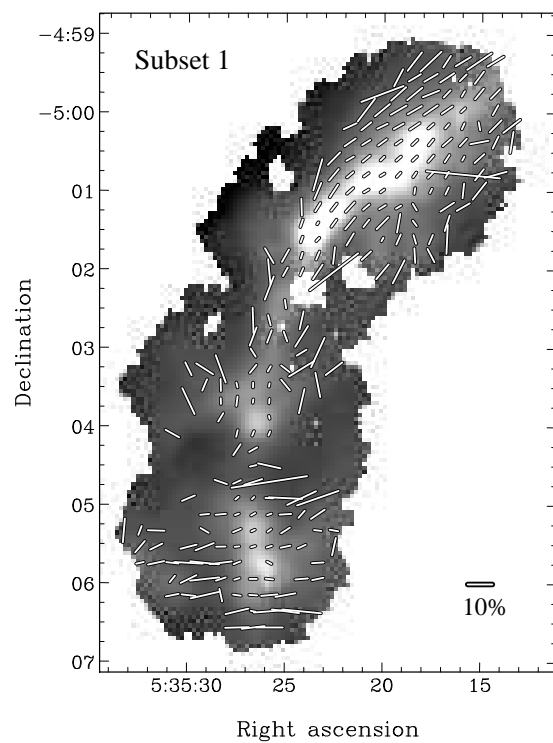












{ 57 }